frontiers in Earth Science

ORIGINAL RESEARCH
published: 30 October 2015
doi: 10.3389/feart.2015.00064

Formation of low-T hydrated silicates in modern microbialites from Mexico and implications for microbial fossilization

Nina Zeyen[1], Karim Benzerara[1], Jinhua Li[1†], Alexis Groleau[2], Etienne Balan[1], Jean-Louis Robert[1], Imène Estève[1], Rosaluz Tavera[3], David Moreira[4] and Purificación López-García[4]*

[1] IMPMC, Sorbonne Universités, UMR Centre National de la Recherche Scientifique 7590, UPMC, MNHN, IRD, Paris, France, [2] IPGP, Sorbonne Paris Cité, UMR 7154, Université Paris Diderot, Centre National de la Recherche Scientifique, Paris, France, [3] Departamento de Ecología y Recursos Naturales, Universidad Nacional Autónoma de México, Mexico City, Mexico, [4] Unité d'Ecologie, Systématique et Evolution, Centre National de la Recherche Scientifique UMR 8079, Université Paris-Sud, Orsay, France

OPEN ACCESS

Edited by:
Dina M. Bower, NASA Goddard Space Flight Center/University of Maryland, USA

Reviewed by:
M. J. L. Coolen, Curtin University, Australia
Christophe Dupraz, Stockholm University, Sweden

***Correspondence:**
Karim Benzerara
karim.benzerara@impmc.upmc.fr

†Present Address:
Jinhua Li, PGL Lab, Key Laboratory of Earth and Planetary Physics, Institute of Geology and Geophysics, Chinese Academy of Sciences, Beijing, China

Specialty section:
This article was submitted to Biogeoscience, a section of the journal Frontiers in Earth Science

Received: *31 July 2015*
Accepted: *13 October 2015*
Published: *30 October 2015*

Citation:
Zeyen N, Benzerara K, Li J, Groleau A, Balan E, Robert J-L, Estève I, Tavera R, Moreira D and López-García P (2015) Formation of low-T hydrated silicates in modern microbialites from Mexico and implications for microbial fossilization. Front. Earth Sci. 3:64. doi: 10.3389/feart.2015.00064

Microbialites are organo-sedimentary rocks found in abundance throughout the geological record back to ~3.5 Ga. Interpretations of the biological and environmental conditions under which they formed rely on comparisons with modern microbialites. Therefore, a better characterization of diverse modern microbialites is crucial to improve such interpretations. Here, we studied modern microbialites from three Mexican alkaline crater lakes: Quechulac, La Preciosa and Atexcac. The geochemical analyses of water solutions showed that they were supersaturated to varying extents with several mineral phases, including aragonite, calcite, hydromagnesite, as well as hydrated Mg-silicates. Consistently, X-ray diffraction (XRD) and Fourier transform infrared spectroscopy (FTIR) analyses revealed that microbialites are composed of a diversity of mineral phases including aragonite and sometimes calcite, hydromagnesite, and more interestingly, a poorly-crystalline hydrated silicate phase. Coupling of scanning electron microscopy (SEM) with energy dispersive X-ray spectrometry microanalyses on polished sections showed that this latter phase is abundant, authigenic, magnesium-rich and sometimes associated with iron and manganese. This mineral phase is similar to kerolite, a hydrated poorly crystalline talc-like phase ($Mg_3Si_4O_{10}(OH)_2 \cdot nH_2O$). Diverse microfossils were permineralized by this silicate phase. Some of them were imaged in 3D by FIB-tomography showing that their morphology was exquisitely preserved down to the few nm-scale. The structural and chemical features of these fossils were further studied using a combination of transmission electron microscopy and scanning transmission X-ray microscopy (STXM) at the carbon and magnesium K-edges and iron $L_{2,3}$-edges. These results showed that organic carbon is pervasively associated with kerolite. Overall, it is suggested that the poorly-crystalline hydrated magnesium-rich silicate forms in many alkaline lakes and has a strong potential for fossilization of microbes and organic matter. Moreover, the frequent occurrence of such an authigenic silicate phase in modern lacustrine microbialites calls for a reappraisal of its potential presence in ancient rocks.

Keywords: microbialites, carbonates, kerolite, STXM, FIB, microfossils

INTRODUCTION

Microbialites are sedimentary structures often composed of carbonates and formed in close association with microorganisms (e.g., Burne and Moore, 1987; Chen and Lee, 2014). They have attracted great attention in Earth sciences for several reasons: first, they are considered as among the oldest traces of life and are found throughout the geological record (e.g., Walter et al., 1980; Buick et al., 1981; Byerly et al., 1986; Hofmann, 2000; Allwood et al., 2006; Lepot et al., 2008; Van Kranendonk et al., 2008). Sometimes they have been also used as a source of information on the metabolic activity of past microbial communities (e.g., Thomazo et al., 2011; Bontognali et al., 2012), in particular cyanobacteria (William Schopf, 2011; Knoll et al., 2013). Second, as refuge areas for the biosphere, microbialites record the history of life and paleoenvironments in the aftermath of biologic crises (Lee et al., 2010; Saint Martin, 2010; Forel et al., 2013). Finally, lacustrine microbialite formations have been suggested as analogs to some hydrocarbon reservoirs such as those discovered in the South Atlantic (Seard et al., 2013). Lacustrine sedimentary rocks are indeed significant sources of hydrocarbons due to their organic enrichment resulting from an optimal combination of primary production, mean water depth and rates of burial (Bohacs et al., 2000).

The mechanisms involved in the formation of ancient microbialites and the conditions in which it occurred, are inferred based on actualism, i.e., the understanding of modern microbialites. It is therefore crucial to improve our current knowledge of modern microbialites. Numerous studies have been conducted on modern marine microbialites, including stromatolites from Shark Bay, Australia (Logan, 1961; Papineau et al., 2005; Allen et al., 2009; Goh et al., 2009) and microbialites from the Bahamas (Reid et al., 2003; Decho et al., 2005; Andres et al., 2006; Baumgartner et al., 2009; Mobberley et al., 2012) as analogs for ancient marine microbialites which are abundant in the Proterozoic record. Fossil lacustrine microbialites are also found in the geological record: e.g., the Eocene Green River formation (Seard et al., 2013) and the Archean Tumbiana formation (Awramik and Buchheim, 2009; Lepot et al., 2009; Stüeken et al., 2015). However, the diversity of formation conditions for modern lacustrine microbialites is much higher than for marine microbialites complicating the search for analogs of ancient systems. Modern lacustrine microbialites are mineralogically diverse: for example, microbialites from Lake Salda Gölü (Turkey) are composed of pure hydromagnesite (Braithwaite and Zedef, 1994), whereas microbialites from Lake Pyramid (Arp et al., 1999) and Lake Searles (Guo and Chafetz, 2012), located in the USA, are composed of aragonite and calcite. Lakes populated by modern microbialites show a broad range of pH from 7.5 for e.g., the Cuatro Ciénegas basin (Mexico) to 10.5 for Lake Bogoria and Lake Magadi (Centeno et al., 2012; Kenya, Harris et al., 2013). Most of these lakes are hypersaline, with salinity values up to 95 g/L for Mono Lake (USA), while some lakes are characterized by moderate salinity including Lake Turkana (Kenya) with salinity as low as 2.5 g/L (Harris et al., 2013). Some studies such as the one by Power et al. (2011) on aragonite microbialites from Clinton Creek (Canada) have established a correlation between the microbialite mineralogy and the chemical composition of the water in which they form. Yet, we need to establish more systematically this relationship between the mineralogy of modern microbialites and the physical and chemical parameters of the solutions so that we can eventually better infer paleoenvironmental conditions in which ancient microbialites formed. Moreover, it is important to describe in detail the traces of life that can be preserved in the mineral fraction of modern microbialites in order to better interpret the potential traces of life detected in fossil samples.

Here, we studied three Mexican crater lakes distant of a few kilometers from each other: Lake Atexcac, Lake Quechulac, and Lake La Preciosa. These lakes are located in the eastern part of the Trans-Mexican Volcanic Belt (TMVB) in the Cuenca de Oriental region. Several studies have been performed on these lakes before, providing hydrological and hydrochemical descriptions of these systems (Vilaclara et al., 1993; Carrasco-Núñez et al., 2007; Armienta et al., 2008; Alcocer and Bernal-Brooks, 2010). Here, we report that all three lakes host modern microbialites that have not been studied before. Interestingly, a nearby lake, Lake Alchichica, also hosts microbialites, which in contrast have been particularly well studied over the last years (Couradeau et al., 2011, 2013; Kaźmierczak et al., 2011; Gérard et al., 2013).

The present study characterizes the microbialites from Lake Atexcac, Lake Quechulac, and Lake La Preciosa with two main objectives. First, we aim to better understand the relationship between their mineralogical composition and the chemical composition of the lakes. Moreover, we document the spatial associations of organic polymers with mineral phases down to the nm-scale and the possible traces of life preserved in the mineral part of the microbialites. For that purpose, we combined a geochemical characterization of the surface water of the three lakes with bulk X-ray diffraction (XRD), Fourier transform infrared spectroscopy (FTIR) and electron and X-ray microscopy analyses of the microbialites. Altogether, these analyses reveal the presence of an authigenic poorly crystalline silicate phase, rich in Mg and sometimes Fe and/or Mn. We discuss the conditions and mechanisms of its formation as well as its importance in the fossilization of microbial communities in lacustrine microbialites.

MATERIALS AND METHODS

Geological Setting

The three investigated crater lakes [Lake Quechulac, Lake La Preciosa, and Lake Atexcac (Figures S1A–C)], belong to the TMVB. TMVB is a continental volcanic arc formed during the Neogene in relationship with the subduction of the Rivera microplate and the northern part of the Cocos plate under the North American plate. This volcanic belt follows an East–West orientation over almost 1000 km (Ferrari et al., 2012). Lakes described in this study are Pleistocene maars located in the Perote area (Puebla State) in the Cuenca de Oriental region, a late Pleistocene to Holocene closed basin located in the eastern part of the TMVB (Armienta et al., 2008). More information can be found on the geology of Lake Atexcac in Carrasco-Núñez

et al. (2007). The lakes are located at an elevation between 2330 m (La Preciosa and Quechulac) and 2360 m (Atexcac) with a maximum depth between 39 m for Lake Atexcac and 45 m for Lake La Preciosa. They are endorheic, closed reservoirs without surface outflow. The climate of the area is temperate with dry winters and annual precipitations around 500 mm/yr. The lakes are considered as oligotrophic (poor in nutrients) and warm monomictic with lake water mixing once per year between January and April (Alcocer and Bernal-Brooks, 2010). With a salinity of 0.45 g/L, Lake Quechulac can be characterized as a freshwater lake following Hammer (1986). Lake La Preciosa is a subsaline lake with a salinity of 1.35 g/L. Lake Atexcac is considered as a hyposaline maar with a salinity of around 7.39 g/L and shows an evaporation rate higher than the rainfall rate and/or a groundwater extraction causing a constant decrease of the water level (Armienta et al., 2008). In all these lakes, we found microbialites with a clotted macrofabric (thrombolites) which, to our knowledge, had not been reported before.

Sample Collection

The field campaign was conducted in January 2012. Microbialites from Lake Quechulac were sampled on a small island located in the middle of the lake (19° 22′ 31.56″N; 97° 21′ 18.29″W) (Figures S1A, D–F). Morphologies of the thrombolites in the lake varied from amalgamated columnar microbialites with a pustular surface (Figure S1D) to partly linked columnar microbialites (Figure S1E) and partly interconnected domal microbialites (Figure S1F). The studied "living" microbialite, i.e., covered by a biofilm (Figure S1F), was sampled beneath the water level. The sample was beige in color with high macro-porosity (Figure S1J). Microbialites from Lake La Preciosa were sampled on the northern shore of the lake (19° 22′ 32.70″N; 97° 23′ 12.14″W). They showed a partly linked columnar morphology and were locally composed of upward directed amalgamated cones (Figure S1G). We studied a sample located above the water level that did not show an apparent biofilm at its surface. It was therefore called "subfossil," although it likely formed very recently. The sample was beige in color with a porosity partly filled by a gray mineral phase (Figure S1K). Microbialites from Lake Atexcac were sampled on the northern inner wall of the lake (19° 20′ 08.27″N; 97° 27′ 10.24″W) (Figures S1C,H,I). These microbialites formed a steep wall superimposed on the crater walls (Figures S1C,H). Microbialites were massive and stratiform and locally characterized by amalgamated columnar microbialites covering the steep cliff (Figure S1I) as observed for Quechulac microbialites. The studied sample was a "living" microbialite, located approximately 50 cm under the water level. The sampled microbialite was gray to beige in color with some macro-porosity (Figure S1L).

Surface water samples were collected from the shore of the lakes at <1 m away from the sampled microbialites. Temperature, pH and specific conductance (conductivity normalized at 25°C) of surface waters of the lakes were measured *in situ*. One hundred milliliters of water were systematically collected from each lake. Water samples were filtered in the same day using 0.22 μm GFF filters and kept in sterile tubes. For major cation analyses, 30 mL of the filtered solutions were acidified. The remaining 70 mL were used for measurements of alkalinity, anionic species and dissolved silica concentration without pre-acidification.

Chemical Analyses of Solutions

The total alkalinity was determined by titration (Gran, 1952) using hydrochloric acid. Commercial mineral water (Evian) was used as a control. Dissolved silica concentration (H_4SiO_4) was measured by continuous flow colorimetric analyses. For these analyses, water samples from Lake Atexcac and Lake La Preciosa were diluted 20 and 10 times, respectively with milli-Q water. Anionic species concentrations (fluorides, chlorides, bromines, nitrates, phosphates and sulfates) were measured by ion chromatography. For these analyses, water samples from Lake Atexcac, La Preciosa, and Quechulac were diluted 100, 20, and 10 times, respectively, with milli-Q water. Inductively coupled plasma atomic emission spectrometry (ICP-AES) was used to determine major cation concentrations (e.g., calcium, magnesium, sodium, and potassium). For these analyses, water samples from Lake La Preciosa, Lake Atexcac, and Lake Quechulac were diluted 200, 150, and 20 times, respectively, with nitric acid at 2%. The uncertainty on alkalinity measurements was better than 1%. Concerning the measurements of dissolved silica, anions, and cations, the uncertainty of the measurements was better than 5%.

Activities of main anions, cations and dissolved silica as well as saturation indices of the surface water solutions of Lake La Preciosa, Lake Quechulac, and Lake Atexcac were calculated using the Visual MINTEQ software. **Table 1** summarizes precipitation equilibrium reactions and solubility constants of the mineral phases included in our calculations, e.g., Ca- and/or Mg-carbonates, sepiolite, "amorphous sepiolite" (as coined by Wollast et al., 1968), kerolite, amorphous silica, and hydroxyapatite. The temperatures of the lakes at the sampling period (e.g., Atexcac: 15.8°C, Quechulac: 15.4°C, La Preciosa: 16.2°C, **Table 2**) were systematically taken into account in the calculation of the saturation indices. The saturation index is defined as the decadic logarithm of the ratio of the ion activity product (IAP) over the solubility constant (Ks):

$$SI = \log (IAP/Ks) \quad (1)$$

The solution is supersaturated with a mineral phase when SI is positive.

Chemical Analyses of Microbialites

Bulk Chemical Analyses

Concentrations of major elements, total organic carbon, and total sulfur were measured by the *Service d'Analyse des Roches et Minéraux* (SARM, Centre de Recherches Pétrographiques et Géochimiques, Nancy, France). About 2 g of ground powders were used for these analyses. Major element analyses were performed using an ICP-AES ICap 6500 (Thermo Fischer) after alkali fusion of rock samples with $LiBO_2$ followed by dissolution in HNO_3. The uncertainties of the major element measurements were between 1 and 25% depending on their concentrations. Organic carbon and total sulfur

TABLE 1 | Precipitation equilibrium reactions of diverse mineral phases and solubility constants used for the calculations of saturation index in the Visual MINTEQ software.

Mineral	Reaction	Log Ks	References
Aragonite	$CaCO_3 + CO_2 + H_2O \leftrightarrows Ca^{2+} + 2HCO_3^-$	−8.34	Plummer and Busenberg, 1982
Calcite	$CaCO_3 + CO_2 + H_2O \leftrightarrows Ca^{2+} + 2HCO_3^-$	−8.48	Plummer and Busenberg, 1982
Vaterite	$CaCO_3 + CO_2 + H_2O \leftrightarrows Ca^{2+} + 2HCO_3^-$	−7.91	Plummer and Busenberg, 1982
Dolomite	$CaMg(CO_3)_2 + 2CO_2 + 2H_2O \leftrightarrows Ca^{2+} + Mg^{2+} + 4HCO_3^-$	−17.09	Ball and Nordstrom, 1991
Hydromagnesite	$Mg_5(CO_3)_4(OH)_2{\cdot}4H_2O \leftrightarrows 5Mg^{2+} + 4CO_3^{2-} + 2OH^- + 4H_2O$	−8.77	Robie and Hemingway, 1973
Sepiolite	$Mg_2Si_3O_{7.5}(OH)\cdot 3H_2O + 4H_3O^+ \leftrightarrows 2Mg^{2+} + 3H_4SiO_4 + 3.5H_2O$	15.76 (crys); 18.78 (am)	Wollast et al., 1968; Stoessell, 1988
Kerolite	$Mg_3Si_4O_{10}(OH)_2{\cdot}H_2O + 6H_3O^+ \leftrightarrows 3Mg^{2+} + 4H_4SiO_4 + 3H_2O$	25.79	Stoessell, 1988
Amorphous silica	$SiO_2 + 3H_2O \leftrightarrows H_4SiO_4 + H_2O$	−2.71	Ball and Nordstrom, 1991
Hydroxyapatite	$Ca_5(PO_4)_3(OH) + H_3O^+ \leftrightarrows 5Ca^{2+} + 3HPO_4^{2-} + 4H_2O$	−57.42	Moreno et al., 1968

TABLE 2 | Physical and chemical properties of the water columns of Lake La Preciosa, Lake Quechulac and Lake Atexcac.

Lake	T (°C)	pH	C_{25} (mS/cm)	Alk (mM)	Ca^{2+} (mM)	Mg^{2+} (mM)	Na^+ (mM)	K^+ (mM)	H_4SiO_4 (mM)	F^- (mM)
La Preciosa	16.2	8.88	2.24	14.1 ± 1%	0.61 ± 5%	8.1 ± 5%	9.0 ± 5%	0.40 ± 5%	0.57 ± 5%	0.045 ± 5%
Quechulac	15.4	8.80	0.84	6.7 ± 1%	0.45 ± 5%	2.4 ± 5%	3.4 ± 5%	0.20 ± 5%	0.21 ± 5%	0.026 ± 5%
Atexcac	15.8	8.75	12.31	30.5 ± 1%	0.62 ± 5%	24.4 ± 5%	80.7 ± 5%	2.93 ± 5%	1.04 ± 5%	0.007 ± 5%

Lake	Cl^- (mM)	Br^- (mM)	NO_3^- (mM)	PO_4^{3-} (mM)	SO_4^{2-} (mM)	HCO_3^- (mM)	CO_3^{2-} (mM)	Bal %	Mg/Ca
La Preciosa	9.4 ± 5%	0.013 ± 5%	0.0199 ± 5%	<0.0008	1.30 ± 5%	13.2	0.5	2.6	13
Quechulac	2.1 ± 5%	0.003 ± 5%	0.0076 ± 5%	<0.0008	0.18 ± 5%	6.3	0.2	0.7	5
Atexcac	107.4 ± 5%	0.166 ± 5%	<0.0004	0.0021 ± 5%	2.06 ± 5%	29.0	0.8	−6.2	39

Concentrations of main cations and anions, dissolved silica (H_4SiO_4) and alkalinity (Alk) are in mmol/L. C_{25} stands for specific conductance of water (conductivity normalized at 25°C). Charge balances (Bal), calculated as 100(Σcations - Σanions)/[(Σcations + Σanions)/2],are in %.*

contents were determined using a carbon/sulfur analyzer Horiba EMIA320V2. The uncertainties of these measurements were better than 10% for sulfur concentration values and for higher carbon concentration values (>0.79%), while the uncertainty of measurements was better than 15% for the carbon concentration of 0.56 wt%. Approximate proportions of mineral phases were calculated in wt% for each microbialite samples. For this purpose, we considered the following stoichiometries: $Mg_3Si_4O_{10}(OH)_2$ for Mg-kerolite and $Fe_2Si_4O_{10}(OH)_2$ for Fe-kerolite.

Microprobe Analyses

Electron probe microanalyses (EPMA) were performed on the silicate phases in microbialite samples from Lake La Preciosa and Lake Atexcac. Analyses were performed on carbon-coated petrographic thin sections. Analyses were performed on a CAMECA S-Five electron microprobe (Camparis, Université Paris 6). Spot analyses were performed at 15 kV and 10 nA in the wavelength-dispersive spectrometry (WDS) mode. We used Fe_2O_3 (Fe), $MnTiO_3$ (Mn, Ti), diopside (Mg, Si), orthoclase (Al, K), anorthite (Ca), and albite (Na) as standards. Quantifications were derived from the automated CAMECA ZAF quantification procedure. Forty-four and 18 spot measurements were performed on the Mg-rich silicate phase and the Fe-Mg-rich silicate phase, respectively. The spot size was around 10–15 μm.

Bulk Mineralogical Analyses of Microbialites

X-ray Diffraction

The bulk mineralogical composition of microbialites was determined by XRD. About 1 g of each microbialite was crushed in an agate mortar and the powder was deposited on an aluminum sample holder. XRD measurements were performed using a Panalytical X'Pert diffractometer equipped with a cobalt anode (Co-Kα). Data were recorded at 45 kV and 35 mA in the continuous-scan mode between 4 and 120° (2θ) with a step of 0.0084° and a total counting time of around 4 h. XRD data were analyzed using the PANalytical X'Pert Highscore software for background subtraction, peak finding, and matching with XRD patterns of reference compounds from the International Crystal Structure Database (ICSD, Fachinformationszentrum Karlsruhe, Germany; US Institute of Standards and Technology, USA).

For additional XRD characterization of the silicate phase, treatments with ethylene glycol were performed. Following the method described by Moore and Reynolds (1997), 1 g of an Atexcac microbialite sample was saturated with pure ethylene glycol overnight in a desiccator before being analyzed by XRD.

Fourier Transform Infrared Spectroscopy Analyses

For FTIR analyses, 2.5 mg of microbialite powder and 300 mg of potassium bromide (KBr) were mixed and ground in an agate mortar. A KBr pellet was prepared for each microbialite sample using a vacuum press under 8 tons of pressure for 1 min. Pellets were placed overnight in a drying oven (95°C) to remove the adsorbed water vapor and were pressed a second time. Transmission spectra were recorded between 400 and 4000 cm^{-1}, using a Nicolet 6700 FTIR spectrometer.

Microscopy Analyses of Microbialites

Sample Preparation for Microscopy Analyses

Samples used for electron and x-ray microscopy analyses were not embedded in resin/epoxy in order to avoid carbon contamination. Fragments of microbialites were sawed then polished down to a ¼of micron with diamond polishing compounds. Then, they were rinsed with ultrasonic cleaning bath in 100% ethanol. Finally, polished sections were dried overnight in a desiccator. Samples were mounted on 2.5 cm wide aluminum sample holders using double-sided carbon tape. Quechulac and La Preciosa microbialite samples were carbon coated. The Atexcac microbialite sample which was further analyzed by scanning transmission x-ray microscopy (STXM) was platinum coated.

Scanning Electron Microscopy

Scanning electron microscopy (SEM) analyses were performed using a Zeiss ultra 55 field emission gun (FEG) SEM. Backscattered electron (BSE) images were acquired using an angle selective backscattered (AsB) detector at an accelerating voltage of 15 kV and a working distance of ∼7.5 mm. The elemental composition of mineral phases was determined by energy dispersive X-ray spectrometry (EDXS) using an EDS QUANTAX detector. EDXS data were analyzed using the ESPRIT software package (Bruker).

Focused Ion Beam Tomography

Focused ion beam (FIB) tomography was performed on a polished-section of the Atexcac microbialite in order to analyze the morphology of the filaments observed in this sample at the few nm-scale. FIB 3D tomography is a technique combining milling of a sample by a Ga^+ ion beam and high resolution imaging by an electron beam. It consists in serial imaging of nano cross-sections of the sample. The sample was first protected from Ga contamination by depositing a 1 μm thick Pt layer. Analyses were performed on a Zeiss Neon40EsB CrossBeam instrument. A volume of 40*10*10 μm was analyzed, with a 20×20×20 nm resolution voxel. Secondary electron images were acquired using a SESI detector at an accelerating voltage of 1.5 kV. A stack of 500 images was collected with a total counting time of 14 h. Analyses were performed using the ImageJ software for alignment, smoothing, and background subtraction for strips removal. Finally, AvizoFire software was used for cropping and computing the volume and imaging the filaments.

Focused Ion Beam Sectioning

Six ultrathin electron-transparent foils were cut from a polished section of a Lake Atexcac microbialite by FIB milling using a FEI Strata Dual-beam 235 instrument operating at 30 kV and 5 nA following the FIB lift-out method described in Bernard et al. (2010). Before milling, a platinum strap was deposited onto the region of interest of the sample. After *in situ* transfer to a copper grid, the foil was thinned down to around 100 nm with a Ga^+ beam current of about 100 pA and at glancing angle.

Transmission Electron Microscopy

FIB foils were analyzed by a JEOL 2100F transmission electron microscope (TEM) operating at 200 kV. This microscope is equipped with a FEG, an ultra-high resolution pole piece, a Gatan energy filter GIF 200, a JEOL detector with an ultrathin windowing detection of light elements, and a scanning TEM (STEM) device, which allows Z-contrast imaging in high angle annular dark field (HAADF) mode. Elemental mapping was acquired by EDXS in the STEM mode. Selected area electron diffraction (SAED) patterns were recorded to check the nature of mineral phases and assess their crystallinity. These analyses were performed after STXM analyses.

Scanning Transmission X-ray Microscopy

The six FIB foils extracted from the Atexcac microbialite sample were analyzed by STXM at the carbon K-edge (C K-edge), the iron $L_{2,3}$-edges (Fe $L_{2,3}$-edges), and the magnesium K-edge (Mg K-edge). Analyses were performed on beamline 11.0.2.2 at the Advanced Light Source (Berkeley, USA), using a 25 nm zone plate. Energy calibration was achieved using the well-resolved 3p Rydberg peak of gaseous CO_2 at 294.96 eV. Data included images and image stacks, from which X-ray absorption near edge structure (XANES) spectra and maps were retrieved. The aXis2000 software (Hitchcock, 2012) was used for data processing. STXM has been used before for the study of biomineralization and fossilization of microbes in ancient and modern microbialites (Benzerara et al., 2006, 2010; Lepot et al., 2009) and experimental samples (Miot et al., 2009; Li et al., 2013, 2014). More details on the principles of STXM and information that can be found in e.g., Bluhm et al. (2006) and Cosmidis and Benzerara (2014).

RESULTS

Aqueous Geochemistry of Lake La Preciosa, Quechulac, and Atexcac

Geochemical analyses of water solutions of the three lakes are summarized in **Table 2**. Ionic balances were better than 7% supporting the consistency of the measurements. Reported water temperatures were similar for all lakes, around 16°C. These lakes were alkaline with a relatively high pH around 8.8 and alkalinity values varying from 6.7 mmol/L for Lake Quechulac up to 30.5 mmol/L for Lake Atexcac. In all cases, bicarbonates made up most of the total alkalinity (**Table 2**).

Concentration of dissolved silica was higher in Lake Atexcac (1.04 mmol/L) than in the other lakes (0.57 mmol/L for Lake La Preciosa and 0.21 mmol/L for Quechulac; **Table 2**).

Saturation indices of the surface waters with several mineral phases were calculated for the three lakes (**Table 3**). All lakes were supersaturated with different Ca-carbonates (calcite, vaterite, and aragonite) as well as dolomite ($CaMg(CO_3)_2$). Lake Atexcac was also supersaturated with hydromagnesite ($Mg_5(CO_3)_4(OH)_2{\cdot}4H_2O$) in contrast to Lake La Preciosa and Lake Quechulac. Finally, all lakes were supersaturated with Mg-silicates.

The surface waters of all lakes were located above the solubility lines of crystalline talc (Jones, 1986), sepiolite, and kerolite (Stoessell, 1988) in a solubility diagram showing the log $(a(Mg^{2+})/a(H^+)^2)$ vs. log $(a(H_4SiO_4))$ of the solutions (**Figure 1**). Only Lake La Preciosa and Lake Atexcac were located above the solubility line of "amorphous sepiolite" as defined by Wollast et al. (1968). Moreover, the representative points of all lakes lay below the solubility line of amorphous silica.

Mineralogical Characterization of the Microbialites

Microbialites from the three lakes had different bulk mineralogical compositions as shown by XRD analyses. La Preciosa microbialites were composed of aragonite mostly and some calcite; Atexcac microbialites were composed of aragonite, calcite and hydromagnesite, while Quechulac microbialites only contained aragonite (**Figure 2**). In addition, XRD patterns of La Preciosa and Atexcac microbialites showed broad peaks located at around 4.5 Å, 2.5 Å, and 1.5 Å. These peaks were consistent with the presence of a poorly crystalline kerolite, a hydrated talc-like phase with the chemical formula $Mg_3Si_4(OH)_{10}$ nH_2O (Brindley, 1977; Léveillé et al., 2000b, 2002; Tosca and Masterson, 2014). However, they were not consistent with sepiolite (Brindley, 1959) or stevensite (Brindley, 1977; Burne et al., 2014). No shift of the peak at 4.5 Å was detected after the ethylene glycol treatment (Figure S2), confirming that kerolite is likely the major Mg-silicate phase in the microbialite. The other Mg-silicate phases may be present in lower abundance as well.

FTIR analyses were consistent with XRD analyses (**Figure 3**, Figures S3, S4). Aragonite was detected in the three lakes based on peaks located at 700 and 713 cm^{-1} (in-plane bending, ν_4CO_3) (Huang and Kerr, 1960; Carteret et al., 2013) and 843 and 855 cm^{-1} (out-of-plane bending, ν_2CO_3) (Carteret et al., 2013). Carbonate symmetric and asymmetric stretching in aragonite were observed at 1084 and 1484 cm^{-1} respectively (Carteret et al., 2013). Calcite was evidenced in Atexcac and La Preciosa by an in-plane bending band at 713 cm^{-1} (ν_4CO_3) and by an out-of-plane bending band at 877 cm^{-1} (ν_2CO_3) (Huang and Kerr, 1960). Hydromagnesite was characterized in Atexcac microbialite by an absorption band located at 595 cm^{-1} due to octahedral vibration (Mg-O), a peak at 797 cm^{-1}, and a peak located at 886 cm^{-1} corresponding to the out-of-plane bending mode of carbonate group (ν_2CO_3) (Farmer, 1974) (**Figure 3**). Moreover, absorption bands at 3448, 3515, 3648 cm^{-1} observed in Atexcac microbialite were interpreted as hydroxyl stretching in hydromagnesite following White (1971) (**Figure 3C**). It should be noted that amorphous silica composing the abundant diatoms observed in the biofilms covering the microbialites may contribute to the broad band observed at 797 cm^{-1} (Tosca and Masterson, 2014). These peaks were only observed in Atexcac microbialites consistently with XRD data. The absorption band at 1020 cm^{-1} (**Figure 3A**, Figures S3B, S4B) observed in microbialites from the three lakes was interpreted as Si-O stretching in tetrahedral vibration in a 2:1 layered configuration of tetrahedral silicate layers and octahedral MgO_6 layers, consistent, but not exclusively, with the presence of kerolite phase (Farmer, 1974; Tosca et al., 2011; Tosca and Masterson, 2014). The lattice vibrations around 460 cm^{-1} observed mostly for Atexcac and La Preciosa microbialite samples (**Figure 3A**, Figure S3A) were attributed to translational OH motions as well as other Si-O vibrations and were consistent with a trioctahedral layer silicate structure similar to that of kerolite (Brindley, 1977; Tosca and Masterson, 2014). Moreover, a trioctahedral occupancy was suggested by the absorption band at 3681 cm^{-1} corresponding to Mg_3-OH stretching vibration (**Figure 3C**; Wilkins and Ito, 1967; Cai et al., 2007; Tosca et al., 2011; Tosca and Masterson, 2014). This absorption band was also present in La Preciosa and Quechulac microbialites at 3679 and 3680 cm^{-1}, respectively, with a smaller intensity for the Quechulac microbialite sample (**Figure 3C**, Figures S3D, S4D).

Bulk analyses of major elements, organic carbon, and total sulfur contents in microbialite samples are summarized in **Table 4**. The presence of aluminum particularly in La Preciosa and Atexcac microbialite samples suggested minor amounts of detrital phases. Interestingly, La Preciosa and Atexcac microbialites contained iron, with Fe_2O_3 concentration of 0.44

TABLE 3 | Saturation indices of the surface water solutions of Lake La Preciosa, Lake Quechulac, and Lake Atexcac for various Ca^- and/or Mg-carbonates, sepiolite, "amorphous sepiolite" as coined by Wollast et al. (1968), kerolite, amorphous silica, and hydroxyapatite.

	La Preciosa	Quechulac	Atexcac
Aragonite $CaCO_3$	1.13	0.79	1.06
Calcite $CaCO_3$	1.28	0.94	1.22
Vaterite $CaCO_3$	0.69	0.35	0.62
Dolomite $CaMg(CO_3)_2$	3.72	2.63	4.03
Hydromagnesite $Mg_5(CO_3)_4(OH)_2{\cdot}4H_2O$	−1.11	−4.73	0.35
Sepiolite $Mg_4Si_6O_{15}(OH)_2{\cdot}6(H_2O)$	4.40	1.95	5.16
Amorphous Sepiolite $Mg_4Si_6O_{15}(OH)_2{\cdot}6(H_2O)$	1.99	−0.40	2.78
Kerolite $Mg_3Si_4O_{10}(OH)_2{\cdot}nH_2O$	7.00	3.63	8.05
Amorphous silica SiO_2	−0.48	−0.92	−0.21
Hydroxyapatite $Ca_5(PO_4)_3(OH)$	−25.55	−25.15	3.26

Saturation indices were calculated using the Visual MINTEQ software. Positive values indicate that solutions are supersaturated.

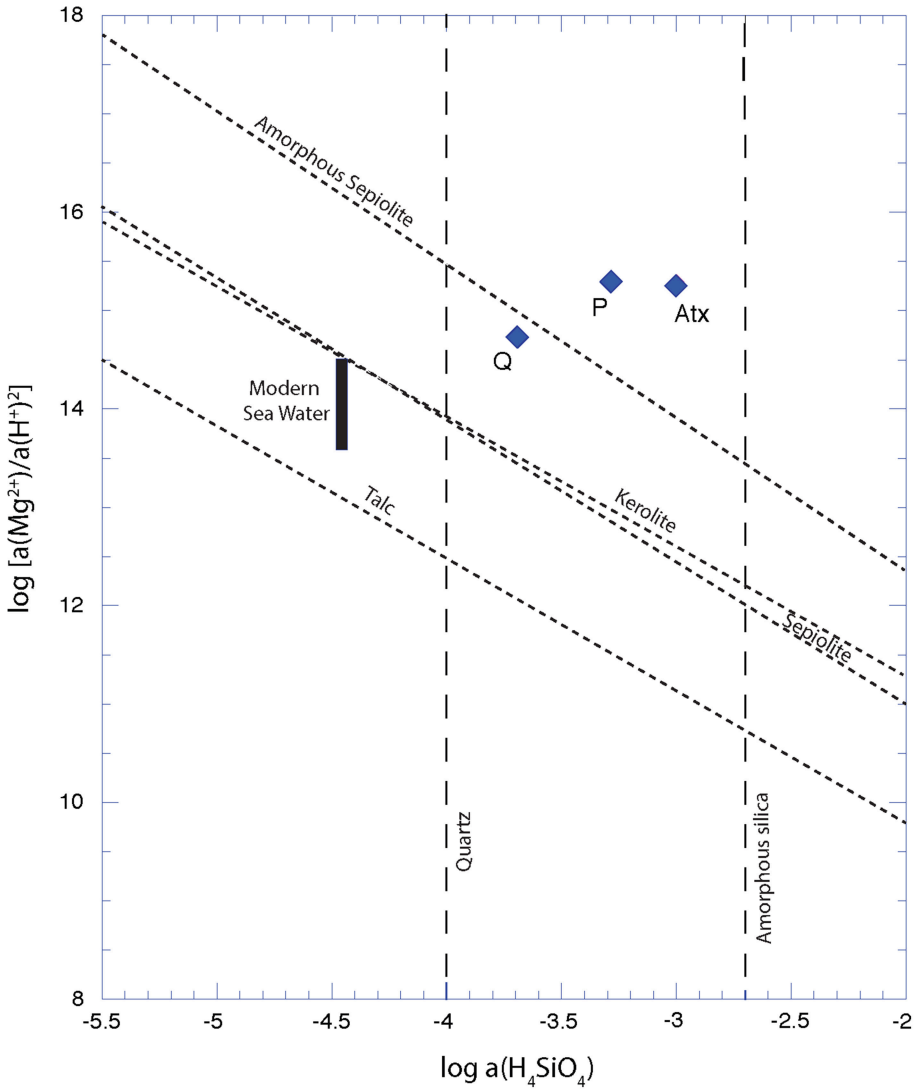

FIGURE 1 | Solubility diagram showing apparent solubilities of different Mg-silicate phases in each lake. Solubility lines of crystalline talc (Jones, 1986), kerolite and sepiolite (Stoessell, 1988), amorphous sepiolite from Wollast et al. (1968) are represented in dashed lines. Diamond points stand for water solutions sampled in Quechulac (Q), La Preciosa (P), and Atexcac (Atx) lakes on January 2012.

± 0.02 wt% and 0.77 ± 0.02 wt%, respectively. The detritic vs. authigenic origin of it is discussed later. Based on these bulk analyses, FTIR and XRD analyses as well as microscopy analyses, approximate proportions of mineral phases were calculated in wt% for each microbialite sample. It was assumed that all calcium was contained in aragonite and/or calcite. Silicon, magnesium, and iron were assumed to be in kerolite for Quechulac and La Preciosa microbialites. In this case, we obtained for La Preciosa microbialite a content of ∼56% of calcium carbonates (aragonite and calcite), ∼43% of Mg-kerolite ($Mg_3Si_4O_{10}(OH)_2$), and ∼1% of Fe-kerolite ($Fe_2Si_4O_{10}(OH)_2$). Concerning Quechulac microbialite, we obtained ∼96% of calcium carbonate (mainly aragonite as shown by XRD analyses) and ∼4% of Mg-kerolite. For Atexcac microbialites, the presence of hydromagnesite made the assessment of the phase proportion more difficult. The chemical composition of Atexcac microbialites could not be accounted for by a mixture of aragonite, hydromagnesite, and kerolite only, but suggested the presence of a silica phase, consistent with FTIR analyses and likely related with the presence of diatoms.

Microscopic Features of Microbialites

The spatial distribution of mineral phases in microbialites was studied by optical microscopy, SEM and electron microprobe. Consistently with XRD and FTIR analyses, microscopy observations showed some mineralogical variability between Quechulac, Atexcac and La Preciosa microbialites. Based on their contrast in the BSE mode and the corresponding EDXS analyses, two main phases were detected in La Preciosa microbialites: Ca-carbonates (aragonite and/or calcite), appearing in bright in

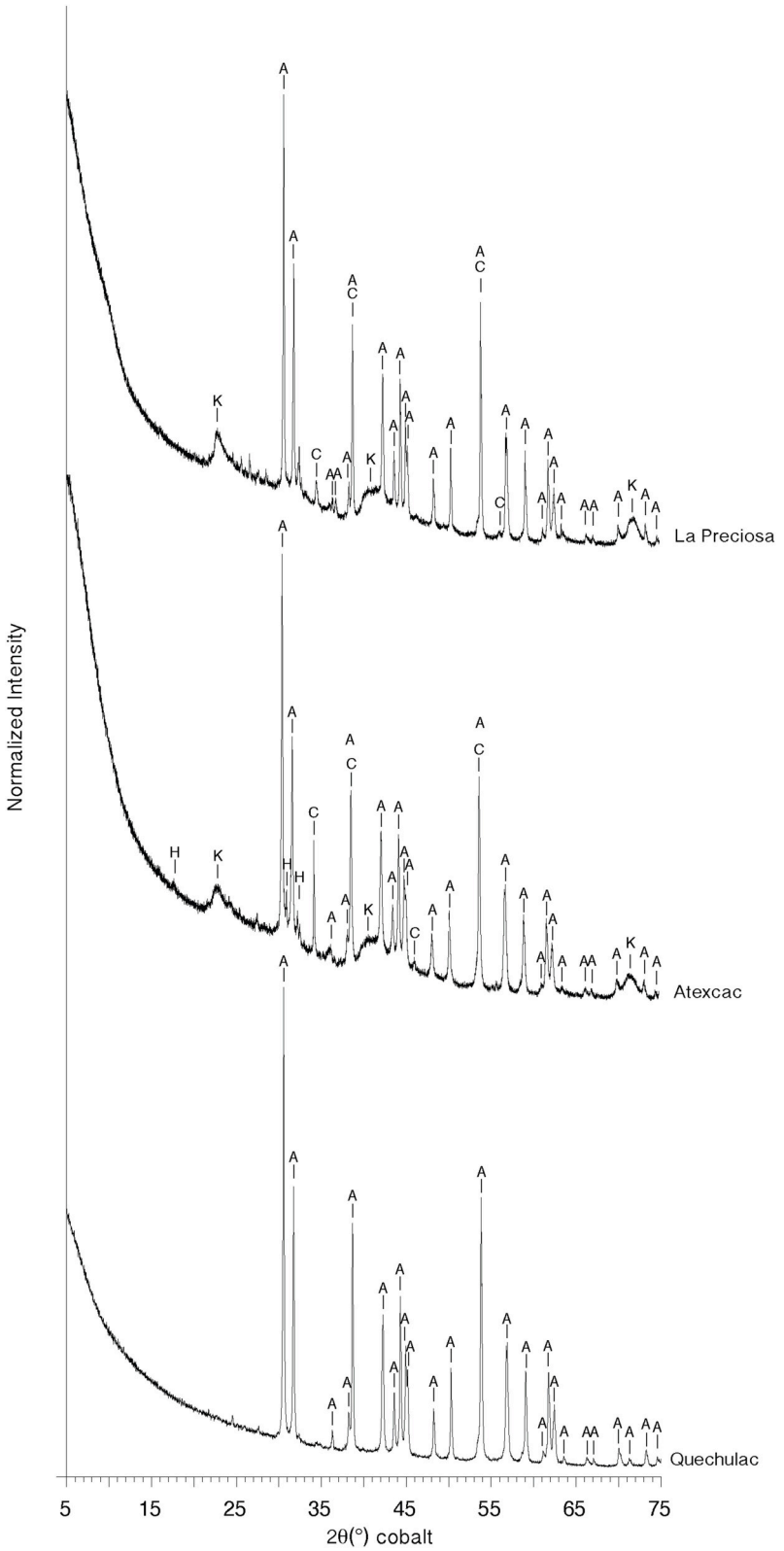

FIGURE 2 | Bulk X-ray diffraction patterns for La Preciosa, Atexcac, and Quechulac microbialite samples. Aragonite (A), calcite (C), and a kerolite phase (K) are identified from the XRD pattern of La Preciosa microbialite. Aragonite (A), calcite (C), hydromagnesite (H), and kerolite (K) can be identified from the Atexcac XRD pattern. Only aragonite (A) can be identified in the Quechulac microbialite XRD pattern.

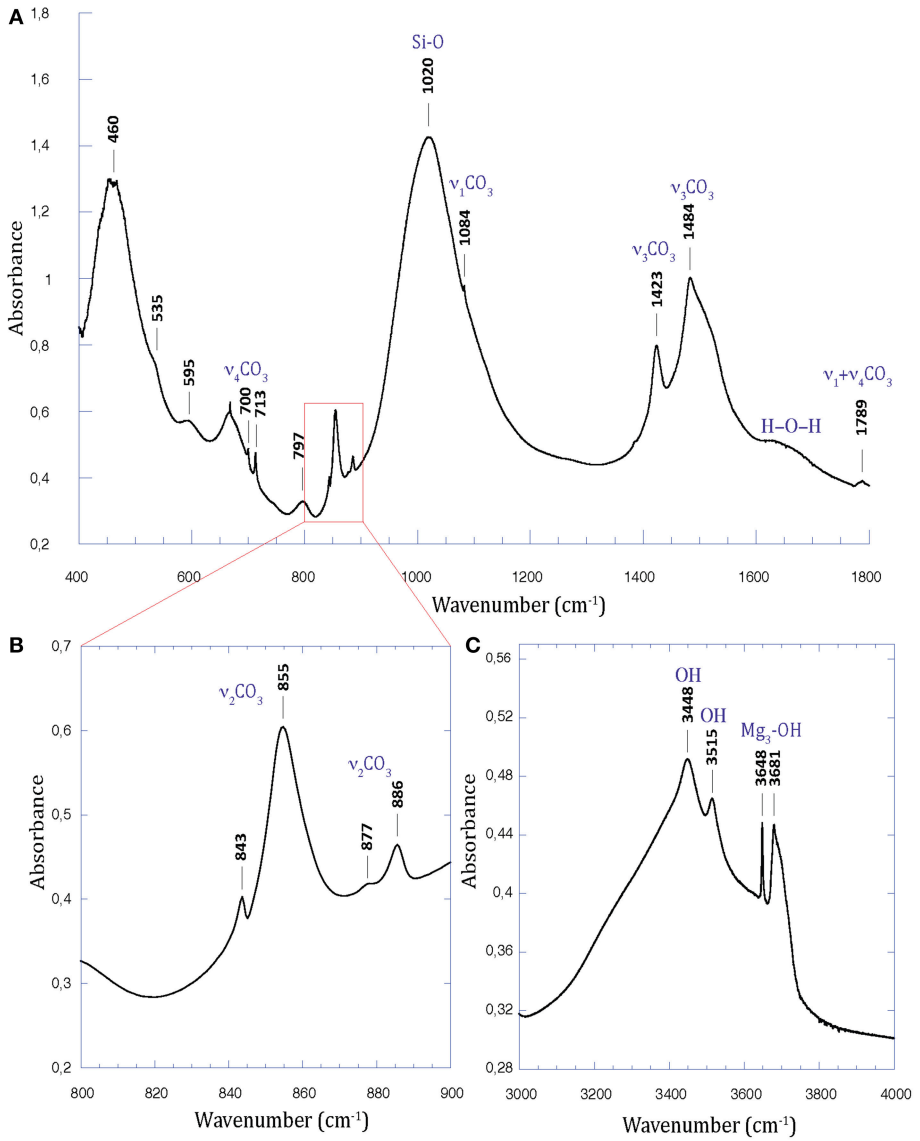

FIGURE 3 | FTIR spectrum of the Atexcac microbialite sample. (A) Spectrum from 400 to 1800 cm^{-1}; **(B)** Close-up over the 800–900 cm^{-1} range; **(C)** Spectrum from 3000 to 4000 cm^{-1}. Note the broad band at 1020 cm^{-1} (Si-O vibrations) and the thinner one at 3681 cm^{-1} (Mg_3-OH stretching) characteristics of kerolite.

the BSE mode and kerolite, appearing in dark gray (**Figure 4**). Magnesium, silicon and oxygen were detected by EDXS in kerolite (**Figure 4C**). Kerolite and Ca-carbonates had a specific distribution in the La Preciosa microbialite: globules of Ca-carbonates measuring several hundred of micrometers in diameter were embedded in a kerolite matrix (**Figure 4A**). Similarly, the Atexcac microbialite sample contained Ca-carbonates patches measuring several hundreds of micrometers and surrounded by a kerolite matrix (Figure S5A). In contrast, the Quechulac microbialite was mainly composed of aragonite, with kerolite appearing as numerous small (<100 μm) patches (Figure S5B).

In optical microscopy, kerolite systematically showed total extinction in crossed polars (**Figure 5**). Based on 44 electron microprobe measurements, a Mg:Si ratio of ~0.77 ± 0.07 was estimated, consistent with the Mg:Si ratio of 3/4 of kerolite (**Table 5**).

Interestingly, replacement and/or embedment of microorganisms by kerolite was systematically observed by SEM in all investigated microbialites. For example, numerous occurrences of very well preserved diatom frustules, replaced by kerolite were evidenced in Atexcac microbialites (**Figure 6**). Kerolite also fossilized dense clusters of morphologically diverse microbial cells. Fossil microorganisms appeared darker in BSE than the kerolite surrounding them. Filamentous and coccoid forms had varying sizes (**Figure 7**). Although it is not possible to infer the number of different species present in these clusters based on morphology only, size distributions are given here for

TABLE 4 | Chemical compositions of microbialites from Lake La Preciosa, Lake Quechulac and Lake Atexcac.

Microbialite Sample	C_{org} wt%	S_{tot} wt%	SiO_2 wt%	Al_2O_3 wt%	Fe_2O_3 wt%	MnO wt%	MgO wt%	CaO wt%	Na_2O wt%	K_2O wt%	TiO_2 wt%	P_2O_5 wt%	LOI wt%	Total wt%
Preciosa	0.81 ± 0.08	0.14 ± 0.01	24.3 ± 0.2	1.20 ± 0.06	0.44 ± 0.02	0.048 ± 0.005	11.7 ± 0.2	26.6 ± 0.5	0.39 ± 0.06	0.20 ± 0.02	0.05 ± 0.01	<0.04	34.39	99.16
Quechulac	0.88 ± 0.09	0.14 ± 0.01	2.2 ± 0.1	0.14 ± 0.01	0.04 ± 0.01	0.007 ± 0.002	1.07 ± 0.05	49.3 ± 0.9	0.14 ± 0.02	0.03 ± 0.01	<0.02	<0.04	46.65	99.55
Atexcac	0.56 ± 0.08	0.16 ± 0.02	29.7 ± 0.3	0.54 ± 0.05	0.77 ± 0.02	0.046 ± 0.005	21.2 ± 0.4	12.7 ± 0.3	0.44 ± 0.07	0.13 ± 0.01	0.03 ± 0.01	<0.04	34.00	99.48

LOI stands for loss on ignition.

indication. Based on 136 measurements, coccoid forms had a diameter varying from 6.1 to 17.7 μm with an average value of 10.4 μm and a standard deviation of 2.1 μm (**Figure 7C**). Based on 119 measurements, the length of filaments ranged between 4.9 μm and 26.2 μm with an average value of 11.8 μm (with a standard deviation of 5.1 μm) and these filaments measured 1.4 μm (with a standard deviation of 0.2 μm) in diameter (**Figure 7D**). Interestingly, microbial assemblages fossilized by kerolite sometimes showed a layered spatial organization with layers composed of coccoid forms and distinct layers composed of filamentous cells sharing the same orientation (**Figures 7B,C**). One layer with filamentous cells was further characterized by FIB-tomography (**Figure 8A**). The filaments were filled by kerolite and their shapes were outlined by a wall, which was dark in BSE mode and corresponded to porosity. 3-D reconstruction of the fossil cells confirmed that filaments shared a similar orientation. Moreover, their tubular structure was relatively well preserved by kerolite down to the few nm-scale (**Figures 8B–D**). The walls surrounding the filaments were not continuous (**Figure 8E**).

One FIB foil was extracted from this area rich in such fossils (Figures S6A,B). STEM observations revealed that the fossils were partially filled by kerolite (Figures S6C–F) and outlined by electron transparent walls (Figure S6B). Organic matter was further characterized at the submicrometer scale by STXM analyses at the carbon K-edge in the 6 FIB foils extracted from Atexcac microbialites (Figures S6F–H). Carbon was pervasively associated with kerolite as attested by carbon maps obtained by subtracting an optical density-converted (OD-converted) image at 280 eV from an OD-converted image taken at 288.6 eV (**Figures 9A–D**, Figures S7A–E). XANES spectra at the C K-edge of carbon associated with kerolite were very similar in all studied FIB foils. They systematically showed peaks indicative of organic functional groups (**Figure 9E** and Figure S7F): a peak at 285.0–285.1 eV, interpreted as 1 s→π* electronic transitions in aromatic and/or olefinic carbon groups (C=C); a peak at 286.7 interpreted as 1 s→π* electronic transitions in carbon in ketone/phenol group (C=O) and a peak at 288.5–288.6 eV interpreted as 1 s→π* transitions in carboxylic C-functional groups (Benzerara et al., 2004; Brandes et al., 2004). The peak at 289.7 eV is interpreted as a 1 s→3p/σ* electronic transitions in carbon in hydroxylated- or ether-linked carbon species. Finally, the peak located at 290.3–290.5 eV is interpreted as carbonate C and/or metal-carboxylic C complexes (Benzerara et al., 2004; Chan et al., 2009). Walls outlining the cells did not contain organic carbon, confirming that they were porous volumes.

Kerolite was further characterized by STEM and STXM analyses at the magnesium K-edge on a FIB foil cut in the Atexcac microbialite. Here, kerolite was observed replacing the silica of a fossil diatom frustule surrounded by Ca-carbonate and hydromagnesite (**Figures 10A–C**). The SAED pattern of the kerolite phase confirmed its poor crystallinity (**Figure 10D**). The XANES spectrum of the kerolite phase at the Mg K-edge showed three main peaks at 1310.7, 1314.6, and 1318.8 eV, the second peak being the most intense (**Figure 10E**). A broader peak was detected at 1333.1 eV. This spectrum was characteristic of Mg in octahedral coordination (Li et al., 1999; Cibin et al., 2003;

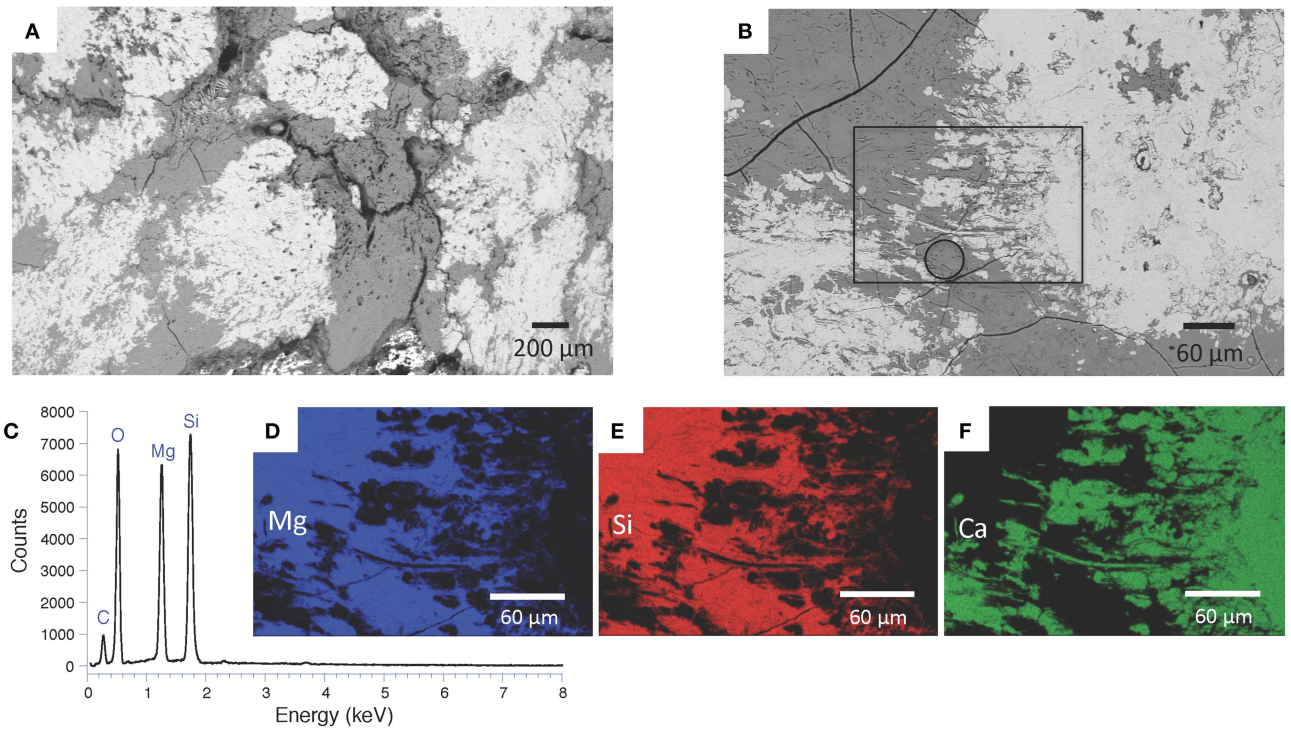

FIGURE 4 | Distribution of mineral phases observed by SEM in the backscattered electron mode on microbialite polished sections of Lake La Preciosa. (A) Global view of Ca-carbonate patches surrounded by a kerolite matrix; **(B)** Close-up view showing the distribution of two Ca-carbonate patches appearing in bright and kerolite appearing in gray; **(C)** SEM-EDXS spectrum of the area marked by a circle in **(B)**, revealing the presence of magnesium and silicon; **(D–F)** EDXS maps of magnesium, silicon, and calcium corresponding to the area marked by a rectangle in **(B)**.

Trcera et al., 2009). Sánchez del Río et al. (2005) noted that some spectral variations may occur due to structural differences. However, based on the existing reference library, it is difficult to identify with this technique any feature that might be specific of kerolite vs. stevensite or sepiolite for example. The XANES spectrum corresponding to hydromagnesite showed a main peak at 1313.6 eV and a smaller one at 1323.5 eV. A kerolite map could therefore be obtained by subtracting an OD-converted image at 1323.5 eV from an OD-converted image taken at 1318.8 eV (**Figure 10F**). This confirmed that hydromagnesite and kerolite were segregated very strictly down to the submicrometer-scale with kerolite replacing the silica of the diatom frustule.

Detection of Fe and/or Mn and Mg-silicates

A poorly crystalline Mg-containing silicate phase similar to the one characterized above but enriched in Mn and/or Fe was sometimes observed in microbialites from Lake Atexcac and la Preciosa (**Figure 11** and Figure S8). STEM observations coupled with EDXS analyses showed that this phase had a different texture than kerolite: kerolite appeared fibrous whereas the Fe, Mg, and Mn rich silicate phase had a smooth texture (**Figure 12**). Electron microprobe analyses showed a (Mg,Fe)/Si ratio equal to 0.82 ± 0.06 in this phase based on 18 measurements (**Table 5**). An iron map was obtained by subtracting an OD-converted image at 700 eV (shown in **Figure 13A**) from an OD-converted image taken at 710 eV (**Figure 13B**). The XANES spectrum, measured in the area rich in Fe showed four main peaks: two peaks at 708.6 eV (L_{3a}) and 710.2 eV (L_{3b}) at the L_3-edge, and two peaks at 721.8 (L_{2a}) and 723.6 (L_{2b}) at the L_2-edge (**Figure 13C**). Based on the measurement of the L_{3b}/L_{3a} intensity ratio and the L_2-edge integral intensity ratio, the $Fe^{3+}/\Sigma Fe$ ratio of this phase was estimated at 65 and 66%, respectively, with a precision inferred to be ±5% by Bourdelle et al. (2013).

DISCUSSION

Authigenic Magnesium Silicates: Abundant and Widespread Mineral Phases

Here, we combined several analytical techniques (XRD, FTIR, SEM, TEM, electron microprobe, and STXM) in order to obtain an accurate characterization of the Mg-silicate phase observed in Mexican microbialites. Such poorly crystalline phases are notoriously difficult to characterize and therefore to identify. This may explain partly why similar occurrences of poorly crystalline Mg-rich silicates in the literature have been attributed to a large diversity of phases: e.g., smectite, stevensite, or kerolite. Alternatively, some of these occurrences are likely distinct phases, and are indicative of varying formation conditions as shown recently by Tosca and Masterson (2014). In Atexcac, Quechulac and La Preciosa, the Mg-silicate phase is poorly crystalline by XRD and SAED; it is Al-poor and has a Mg:Si stoichiometry around 3:4; Mg is in octahedral coordination in this phase.

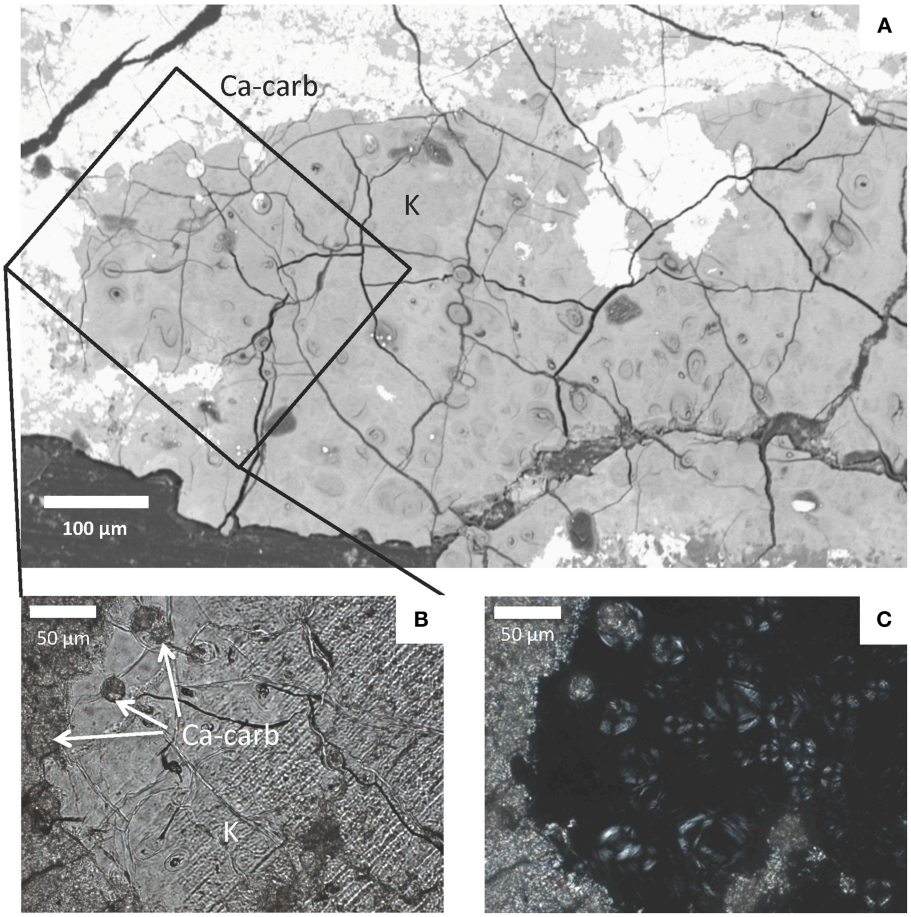

FIGURE 5 | Light and electron microscopy observations of the Atexcac microbialite. (A) SEM micrograph in the backscattered electron mode. Bright areas correspond to Ca-carbonate (Ca-carb) and gray areas to kerolite (K); **(B)** Photomicrograph in transmitted light (parallel polars) of Atexcac microbialite thin section corresponding to the area marked by a rectangle in **(A)** and showing the distribution of Ca-carbonate appearing in darker gray (Ca-carb) and kerolite (K) appearing in light gray; **(C)** Photomicrograph on the same area as in **(B)** in crossed polars showing that the kerolite phase is poorly crystalline at this scale.

TABLE 5 | Electron microprobe analyses performed on the kerolite phase and the Fe-rich silicate phase in the Atexcac and La Preciosa microbialites.

	Mg-Si Areas (44 Measurement points)			Mg-Fe-Si Areas (18 measurement points)			
	[Mg] (at%)	[Si] (at%)	Mg/Si	[Mg] (at%)	[Fe] (at%)	[Si] (at%)	(Mg,Fe)/Si
Average (% at)	16.53	21.60	0.77	15.14	2.09	21.15	0.82
Standard deviation (%at)	1.01	0.74	0.07	0.90	0.87	0.69	0.06

Sometimes, it is associated with large amounts of Fe and/or Mn; however, in that case, it is not clear whether this is the same phase as the pure Mg-phase. XRD and the Mg:Si stoichiometry are not consistent with sepiolite. Because the phase evidenced by XRD is non-swelling, it is more likely kerolite following Léveillé et al. (2000b, 2002).

Moreover, we showed that kerolite is very abundant in Atexcac and La Preciosa microbialite samples and is authigenic as attested by the replacement of amorphous silica in diatom frustules or permineralization of microorganisms in fossil biofilms. It has been shown accordingly by some previous experimental studies that poorly crystalline kerolite can precipitate in adequate solutions at room temperature (e.g., Tosca and Masterson, 2014).

Although the significance of authigenic Mg-silicates remains often underemphasized, it is important to note that they have been repeatedly described in several kinds of formations and in a wide diversity of environments: for example, stevensite (trioctahedral smectite, $(Ca,Na)_xMg_{3-x}(Si_4O_{10})(OH)_2$) has been described in association with aragonite in salt deposits of the alkaline Lake Yoa, Chad (Darragi and Tardy, 1987), or replacing diatom frustules in several Bolivian saline lakes in the Altiplano (Badaut and Risacher, 1983). Furquim et al. (2008) reported

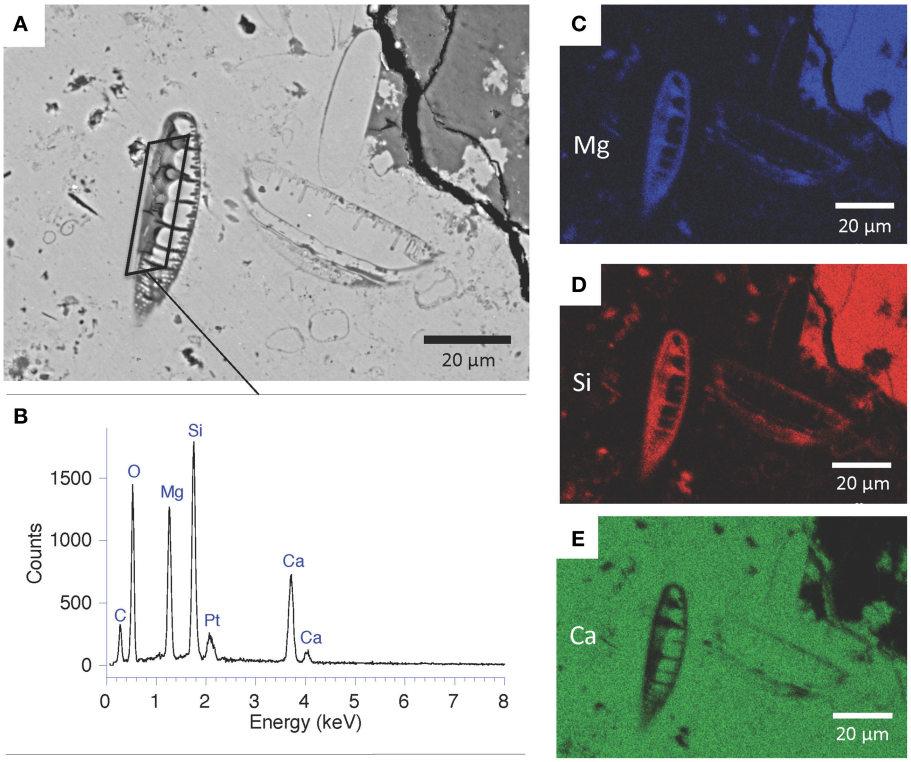

FIGURE 6 | SEM analyses of fossil diatoms enclosed in Ca-carbonate and replaced by kerolite in Atexcac microbialite. (A) SEM micrograph in the backscattered electron mode. Two diatom frustules can be recognized in the center of the image; **(B)** SEM-EDXS spectrum of the area outlined in **(A)**. Platinum was deposited to conduct surface charges upon observations; **(C–E)** EDXS maps of magnesium, silicon, and calcium showing two diatoms replaced by a Mg-silicate phase.

authigenic di- and trioctaedral smectites in soils surrounding the alkaline-saline Lake Nhecolândia in Brazil. An amorphous Mg-silicate has been observed in association with EPS in the coastal sabkha of Abu Dhabi (United Arab Emirates), and it has been interpreted as a precursor phase evolving to dolomite (Bontognali et al., 2010). A Mg-Fe silicate phase has been observed in association with calcite and aragonite in hotsprings in the Ruidian geothermal area, China (Jones and Peng, 2014), and Fe-rich smectites (named nontronite in the literature) have been described in deep-sea sediments from Iheya Basin, Japan (Ueshima and Tazaki, 2001).

Importantly, authigenic magnesium silicates have also been observed in several modern lacustrine microbialites: (1) in Mono Lake, a saline and alkaline lake in California (Souza-Egipsy et al., 2005); (2) in the crater Lake of Satonda, Indonesia (Arp et al., 2003; Benzerara et al., 2010); (3) in basaltic caves at Kauai (Hawaii) (Léveillé et al., 2000a,b, 2002, 2007); (4) in the alkaline and hyposaline Lake Clifton in Western Australia (Burne et al., 2014); and finally (5) in the alkaline and saline Lake Van, Turkey (Kempe et al., 1991; López-García et al., 2005; Benzerara et al., 2006), where the formation of a Mg-silicate phase was indirectly suggested by hydrochemistry study (Reimer et al., 2009). Therefore, the three Mexican lakes described here add to the list of such authigenic magnesium silicate occurrences in modern lacustrine microbialites. Here, we show that the phase can have diverse textures: it sometimes replaces diatom frustules or biofilms; it often forms laminas or patches within microbialites. FTIR and SEM were the most efficient tools to detect this phase, whereas its detection was not systematic by XRD. Therefore, some studies may have overlooked this mineral phase. These analytical issues and the fact that all the lakes mentioned above cover a relatively wide diversity of chemical conditions for microbialite-harboring alkaline lakes suggest that this phase is likely more common in lacustrine microbialites than previously thought.

Last but not least, such authigenic magnesium silicate phases have been observed in some ancient marine and lacustrine formations showing that they can be traced back in the geological record. For example, Tosca et al. (2011) reported occurrence of talc in two early Neoproterozoic carbonate formations located in the Akademikerbreen Group, Svalbard and in the upper Fifteen mile Group of the Ogilvie Mountains (NW Canada) which they interpreted as the product of dehydration of authigenic hydrous Mg-silicates, including kerolite. Similarly, Sánchez-Navas et al. (1998) reported the occurrence of authigenic poorly crystalline Fe- and Al-rich smectite in Upper Jurassic marine phosphate stromatolites in the Almola Sierra (Serranía de Ronda, SW Spain) that they also interpreted as the product of crystallization of

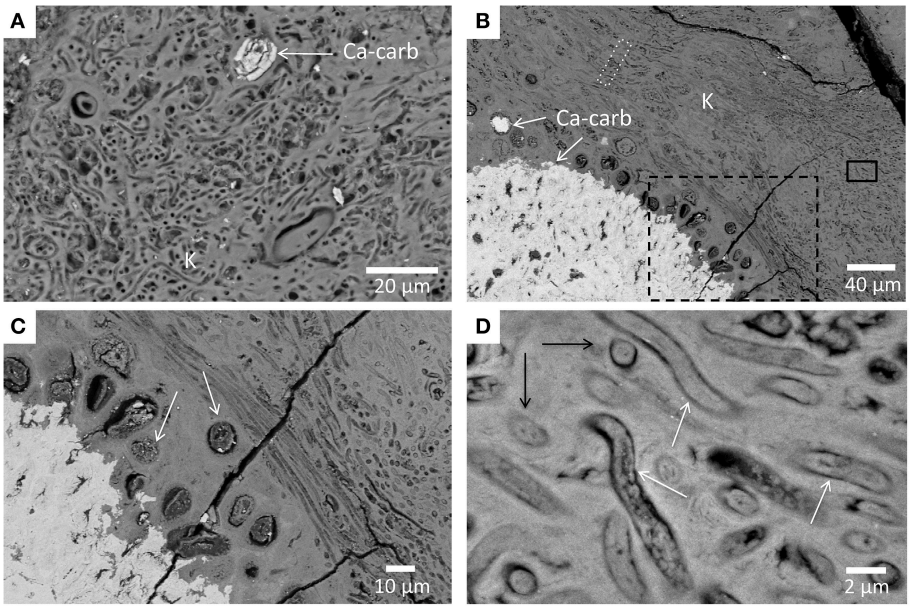

FIGURE 7 | SEM-backscattered images of the microbial biofilm fossilized by the magnesium silicate phase. (A) Quechulac microbialite polished section. Ca-carbonate appears in bright (Ca-carb) but most of the area is composed of kerolite (K) appearing in light gray. Filamentous and coccoid forms appear in darker gray; **(B)** Atexcac microbialite polished section; **(C)** Magnified area from the dashed rectangle in **(B)** showing coccoids (white arrows) of varying sizes; **(D)** Magnified area from the black rectangle in **(B)** showing several filaments with varying lengths (white arrows) and cross-sections of these filaments (black arrows).

authigenic Al-Si-Fe gels. Recently, Wright and Barnett (2015) described Mg-silicates in some South Atlantic early Cretaceous lacustrine carbonates from offshore Brazil, the biogenicity of which they discussed in detail. Finally, authigenic magnesium-silicates were described in several lithofacies in the Eocene lacustrine Green River formation (Bradley and Eugster, 1969; Tank, 1972; Dyni, 1976).

More generally, some Mg-rich silicates have often been observed in ancient microbialites but they have usually been interpreted as detrital phases. For example, Fe-rich chlorites have been observed in 2.7 Ga old stromatolites from the Tumbiana formation (Lepot et al., 2009). In these stromatolites, chlorite sometimes occurs as micro- to nanoscale crystals with a cryptocrystalline web-like texture and contains diffuse organic matter (Lepot et al., 2009). Since Tumbiana stromatolites are increasingly interpreted as lacustrine (e.g., Stüeken et al., 2015), the possibility that chlorite derives from an authigenic Mg-silicate phase can be evoked. One key issue for future studies will be to understand how authigenic Mg- and/or Mn and Fe-containing silicate phases transform with diagenesis and metamorphism and what information about the initial phases can be retrieved from the final products. Interestingly, experiments conducted by Whitney and Eberl (1982) showed that gels with a Mg:Si ratio identical to that of talc transformed to stevensite at temperatures between 300 and 450°C. In aluminum-containing systems at 400–450°C, stevensite continued to react to form a perfectly ordered mixed-layer stevensite/chlorite. Overall, at least part of the chlorite observed in Tumbiana stromatolites may therefore derives from an authigenic precursor similar to those observed in modern microbialites. We do not claim here that authigenic Mg-silicates are responsible for the fossilization of all microbes in fossil microbialites. Based on our current knowledge, it might actually be anecdotic. However, based on the modern record, we think that this possibility should be more carefully and systematically addressed when studying ancient samples.

Environmental Conditions Required for Kerolite Precipitation

Kerolite precipitation equilibrium can be summarized by the following reaction (2):

$$Mg_3Si_4O_{10}(OH)_2 \cdot H_2O + 6H_3O^+ \leftrightarrows 3Mg^{2+} + 4H_4SiO_4 + 3H_2O \quad (2)$$

$$\text{With } Ks = (a(Mg^{2+})^3 \cdot a(H_4SiO_4)^4) \,/\, a(H_3O^+)^6 \quad (3)$$

where Ks is the solubility constant of kerolite, and a() denote the species activities.

Stoessell (1988) determined a Ks of 25.79 ± 0.24 for kerolite by conducting dissolution experiments over time periods approaching 10 years at 25°C and 1 atm. As suggested by Equation (3), three parameters can favor kerolite precipitation and possibly explain the formation of this phase in the Mexican microbialites: high pH, high dissolved silica activity and high magnesium activity. Tosca et al. (2011) have stressed the importance of pH as a main factor controlling the precipitation of magnesium silicates. They established a pH boundary at 8.7 above which poorly crystalline Mg-silicate can precipitate in solution with salinities close to that of seawater (35 g/L). Similarly, Badaut and Risacher (1983) argued that variations in

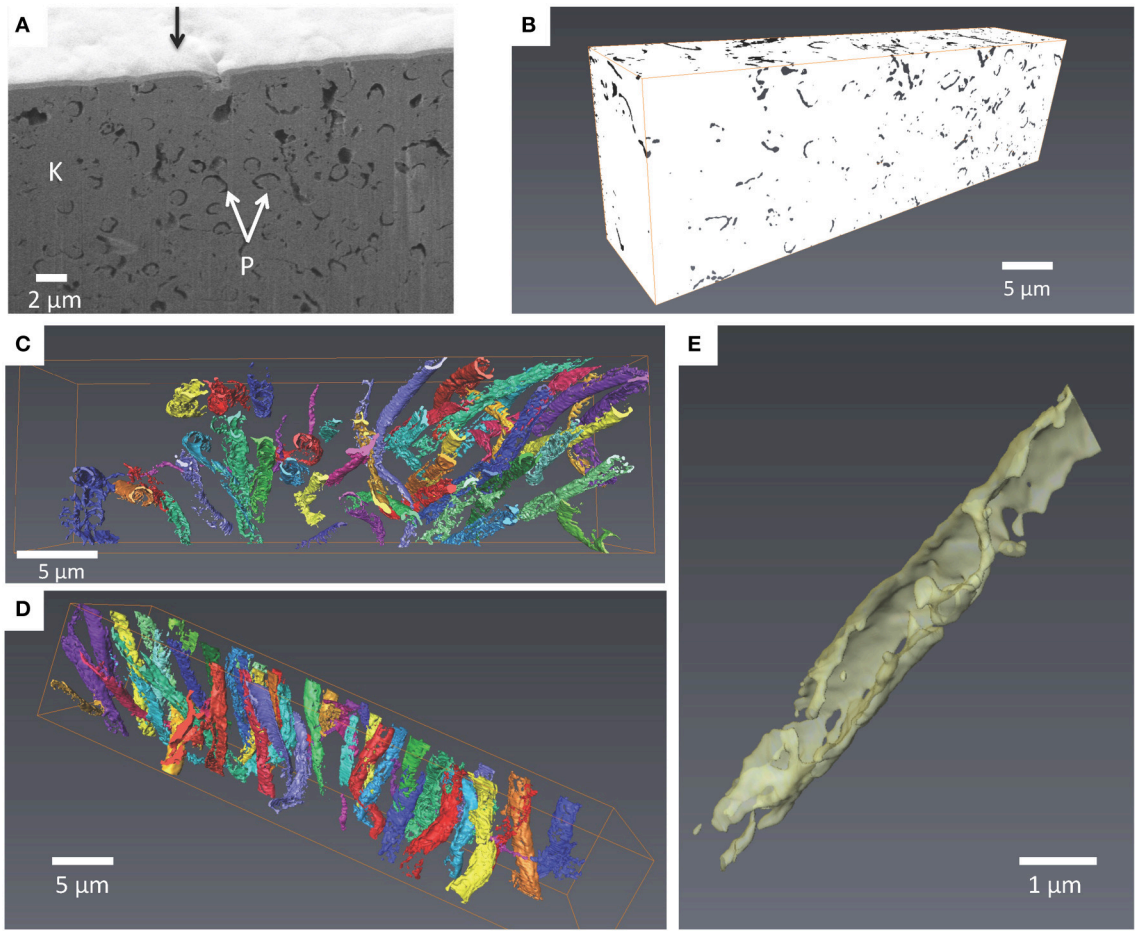

FIGURE 8 | FIB 3D tomography of filaments observed in the Atexcac microbialite. (A) SEM image in the secondary electron mode of a vertical wall excavated by FIB milling perpendicular to the sample surface (see white dotted rectangle in **Figure 7B**). The sample surface has first been covered by a 1 µm thick Pt layer deposit (black arrow); fossil cells are outlined by a seemingly porous walls (P) which are darker than kerolite (K); **(B)** Volume rendering after alignment, smoothing, and binarisation of the images. Porous walls are now colored with one color for each filament (volume considered: 35*10*7 µm); **(C)** 3-D back view of filaments; **(D)** 3-D top view of filaments crossing the studied volume; **(E)** Close-up on a filament. The wall is not continuous.

the Mg concentration as observed in natural environments have a minor effect, but saturation with respect to amorphous silica and a pH above 8.2 were two main conditions required for the formation of authigenic smectite at 5°C.

In our study, two of the three lakes were particularly rich in dissolved silica (1.04 mmol/L and 0.57 mmol/L for Lake Atexcac and Lake La Preciosa, respectively), but below the saturation of amorphous silica and contained microbialites with high kerolite contents. The three lakes (La Preciosa, Atexcac, and Quechulac) had a pH around 8.8 and were located above the kerolite solubility line at the time when samples were collected. La Preciosa and Atexcac solutions were also above the solubility lines of sepiolite, kerolite, and talc (**Figure 1**). Quechulac solution was above the solubility lines of the same phases except "amorphous sepiolite," an awkward term coined by Wollast et al. (1968) to refer to a structurally undefined phase. Mineralogical analyses strongly suggest that the major phase observed in the Mexican microbialites is similar to kerolite, which is therefore consistent with the observed supersaturation of the solutions (**Table 3**). Two questions remain open. First, it will be important to determine in the future how much the solubility line of kerolite depends on the crystalline order of the phase and/or the extent of its association with organic matter. Second, reconciling the mineralogical composition of the microbialites with the chemical composition of the lake waters is not straightforward. Indeed, mineral phases in the microbialites may have formed continuously or discretely over a certain period of time, whereas the chemical composition of the lake was measured during sample collection only. Several earlier studies have monitored the chemical composition of surface water in Lakes of Atexcac, La Preciosa, and Quechulac at different periods during the year (Vilaclara et al., 1993; Armienta et al., 2008; Kaźmierczak et al., 2011). Comparison with present data suggests that the solution chemistry of these lakes has not varied significantly over time and that these lakes have been supersaturated with respect to kerolite at least since 2001 (Armienta et al., 2008). Yet, the

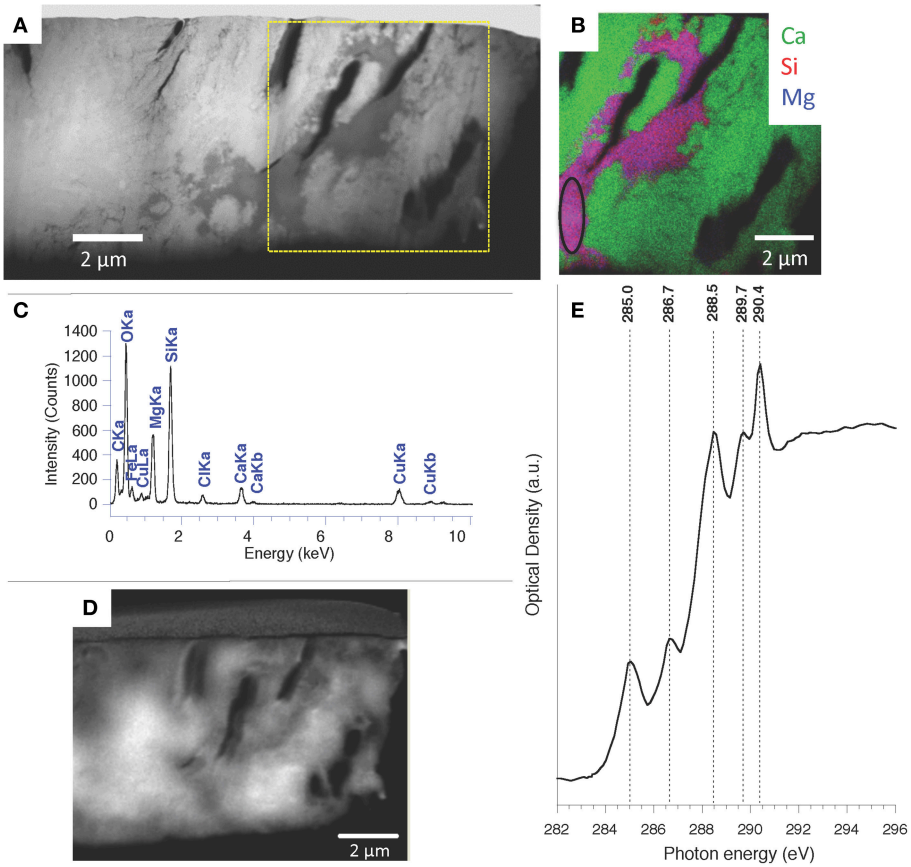

FIGURE 9 | TEM and STXM analyses at the C K-edge performed on one Atexcac microbialite FIB foil. (A) HAADF-STEM image; **(B)** STEM-EDXS map of Ca, Si, and Mg performed on the square area in **(A)**; **(C)** EDXS spectrum corresponding to the kerolite area circled on **(B)**; **(D)** Organic carbon map obtained by subtracting an optical density-converted (OD-converted) image at 280 eV from an OD-converted image taken at 288.6 eV; **(E)** XANES spectrum at the C K-edge from the area outlined in **(B)**. Labelling of the peaks: 1 s→3p/σ^* electronic transitions in carbon in aromatic or olefinic carbon groups (C=C) at 285.0 eV; 1 s→3p/σ^* transitions in ketone/phenol (C=O) C-functional group at 286.7 eV; 1 s→3p/σ^* transitions in carboxylic C-functional groups at 288.5 eV; C1 s→3p/s* electronic transitions in carbon in hydroxylated- or ether-linked carbon species at 289.7 eV; carbonate C and/or metal-carboxylic C complexes at 290.4 eV.

chemical composition of the Mexican lakes may vary temporarily depending on seasons because of the mixing of the water column once per year and/or high influxes during rain events of fine volcanic material that dissolves easily in high pH water and raise temporarily Mg and SiO_2 activities. It is therefore possible that kerolite forms preferentially at these specific moments and only highly frequent water sampling may provide further information on that issue.

The Environmental Message Conveyed by the Enrichment of Authigenic Silicates in Fe and Mn

The present study showed that authigenic silicates forming in Mexican microbialites sometimes contained high concentrations of iron and/or manganese. These elements may compose separate phases mixed with kerolite. However, the relatively homogenous Fe and Mn distribution observed down to the nm-scale, with a relatively constant (Mg+Fe+Mn)/Si ratio (0.82 ± 0.06) close to the Mg/Si ratio measured in kerolite, suggests that Mn and Fe substitute in the silicate phase structure. The replacement of Mg by divalent Fe in the talc structure has been studied previously by FTIR analyses (Wilkins and Ito, 1967; Farmer, 1974). This replacement leads to a shift of the 3677 cm^{-1} band of talc to 3663.5 cm^{-1}, characteristic of the MgMgFe-OH vibrations (Wilkins and Ito, 1967; Farmer, 1974). However, this absorption band was not observed in our bulk spectra, probably due to the low abundance of this phase in the microbialite samples.

Some Al-poor and Fe-rich authigenic silicate phases have been described previously. For example, greenalite ($(Fe)_3Si_2O_5(OH)_4$) is a silicate phase with structural Fe, which has been described in ancient sediments, such as banded iron formations (BIFs) (Kaufman, 1996; Konhauser et al., 2007). Minnesotaite ($(Fe,Mg)_3Si_4O_{10}(OH)_2$) (Kaufman, 1996) and grunerite $Fe_7Si_8O_{22}(OH)_2$ (Nayak et al., 2011) are additional phases which may result partly from greenalite transformation upon diagenesis or metamorphism. The poorly crystalline Fe- and Mg-rich silicate phase observed in modern Mexican microbialites might be a precursor of greenalite.

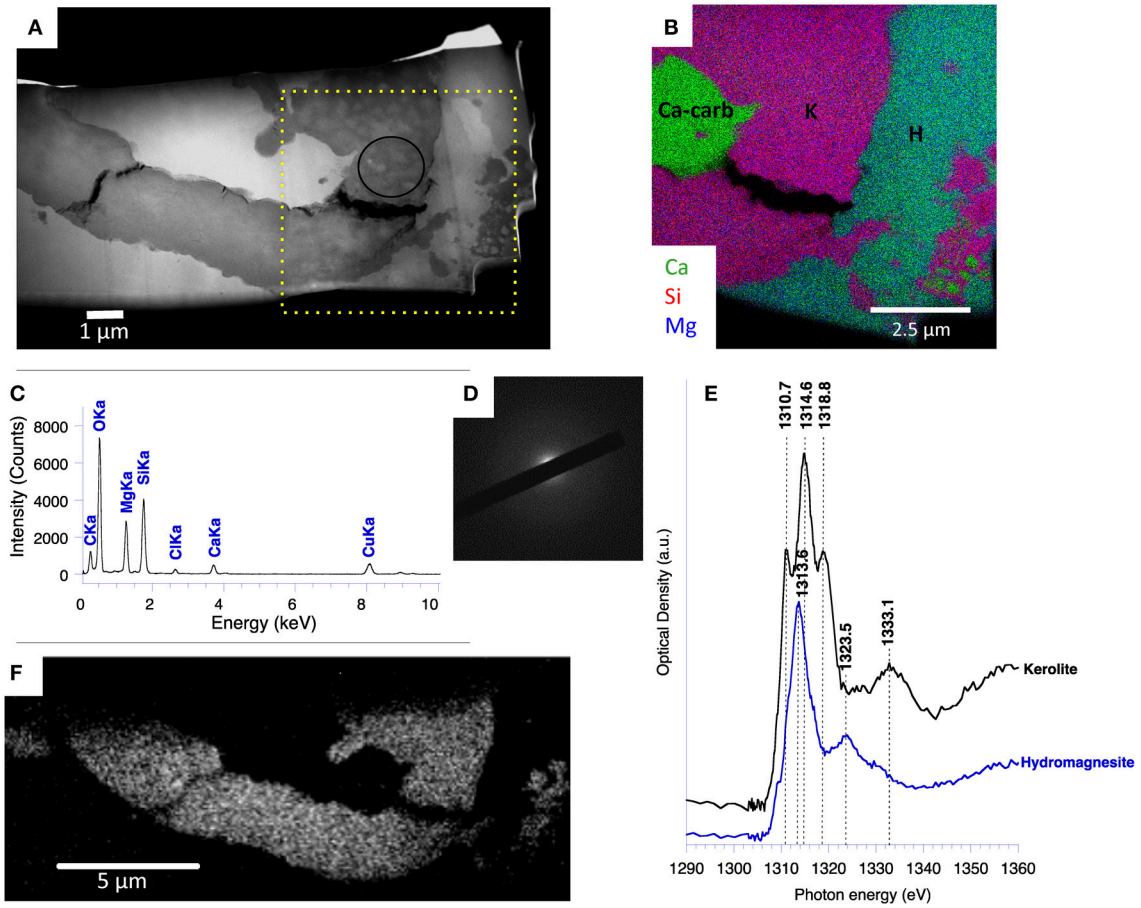

FIGURE 10 | STEM and STXM analyses at the Mg K-edge performed on a fossil diatom of the Atexcac microbialite. (A) HAADF STEM image; **(B)** STEM-EDXS map of Ca, Si, and Mg performed on the square area on **(A)** showing the distribution of Ca-carbonate (Ca-carb), kerolite (K), and hydromagnesite (H); **(C)** EDXS spectrum corresponding to the kerolite area circled on **(A)**; **(D)** SAED pattern obtained from the area circled on **(A)** and corresponding to the kerolite phase showing no diffraction arc; **(E)** XANES spectra at the Mg K-edge of kerolite and hydromagnesite; **(F)** Map of magnesium specifically associated with kerolite obtained by subtracting an OD-converted image at 1323.5 eV from an OD-converted image taken at 1318.8 eV.

High concentrations of Fe and Mn in authigenic silicates in the surface microbialites studied here indicate that the lakes contained high Fe and Mn concentrations when authigenesis occurred. Microorganisms might change the redox, hence the solubility of Fe by their metabolic activity within the biofilms but Fe has first to be delivered to the biofilm. Therefore, Fe enrichment in microbialites indicates a change in the water composition primarily. Part of the Fe composing the authigenic silicates is divalent. However, it is possible that it was pure Fe(II) when precipitation occurred and that Fe was subsequently oxidized within the silicate phase, in contact with oxic water. High Fe concentrations in solutions at a pH higher than 8.5 and under oxic conditions are surprising considering the low solubility of Fe under these conditions (e.g., Schwertmann, 1991). Three hypotheses can be formulated to explain temporary high Fe and Mn concentrations at shallow depths in Mexican lakes. First, seasonal mixing of the water column in winter may bring to the surface deep and anoxic waters loaded with Fe(II). Second, a punctual influx of Fe-rich volcanic rocks which are abundant on the lake shores, e.g., during the rainy season, may bring high amounts of material that dissolve quickly at high pH and release high concentrations of Fe and Mn at shallow depths of the lakes. Finally, local groundwater vents may release at shallow depth high concentrations of Fe and Mn. Finding tracers of these different sources would be important to discriminate between these different scenarios and infer the potential rhythmicity of Fe and Mn enrichments in these rocks.

The Strong Potential of Kerolite for Fossilization of Microorganisms

Here, we observed an excellent morphological preservation of a relatively large diversity of microorganisms by kerolite down to the nm-scale. First, we detected several diatom frustules replaced by kerolite in the microbialites. All three lakes are undersaturated with amorphous silica, and it is known that living diatoms are able to form their frustules under these conditions (Perry, 2003). However, once diatoms die, their frustules should dissolve (Wollast, 1974) and only few fossil traces should be

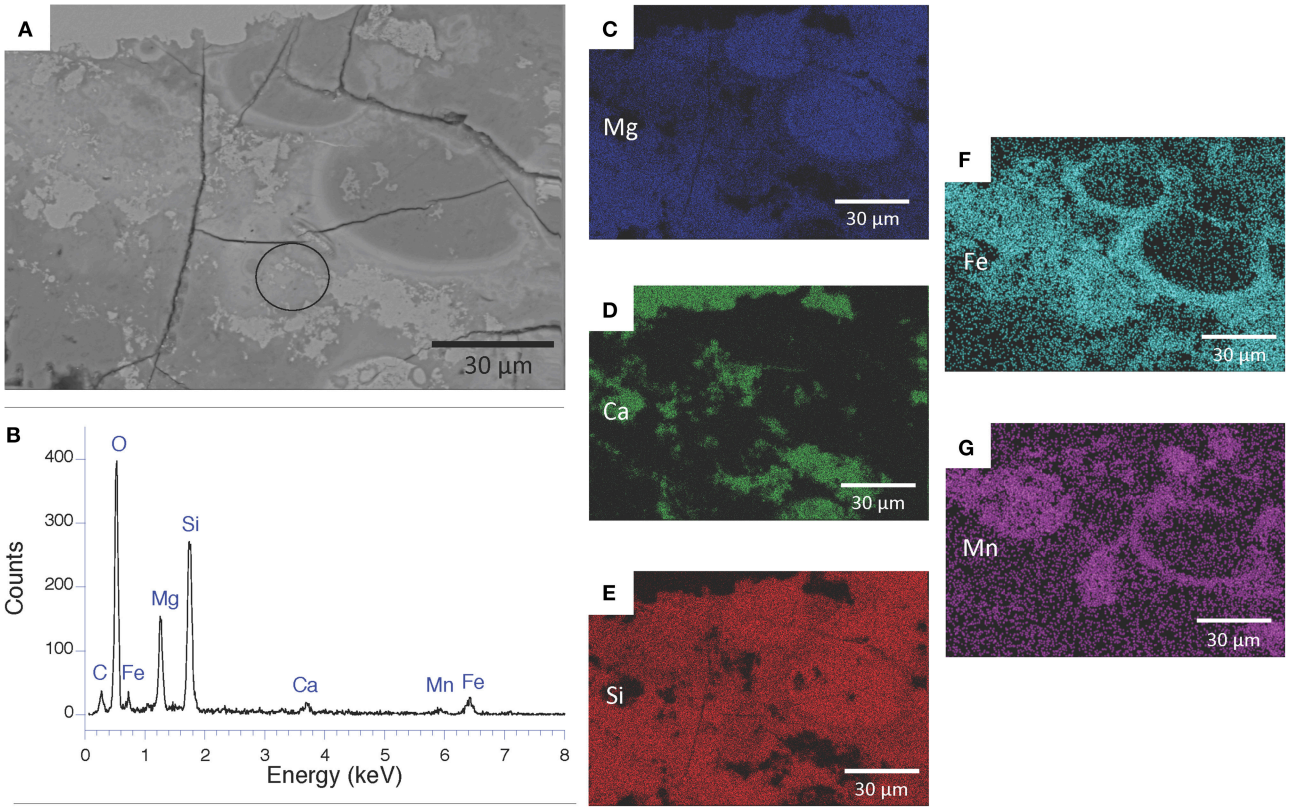

FIGURE 11 | Distribution of Fe and Mn in silicates of the Atexcac microbialite. (A) SEM micrograph in backscattered electron mode; **(B)** SEM-EDXS spectrum of the area circled on **(A)**; **(C–G)** EDXS-maps of magnesium, calcium, silicon, iron, and manganese. Ca is anticorrelated with all the other elements and associated with Ca-carbonates (aragonite and/or calcite). Silicon is systematically associated with magnesium and sometimes iron and manganese.

left in the mineral part of microbialites. Accordingly, we never observed fossil diatoms with a silica frustule. Alternatively, all the diatom frustules that could be recognized morphologically were replaced by kerolite. Several mechanisms favoring diatom frustule preservation have been studied in the past, explaining how lacustrine diatomite or marine diatom and radiolarian sediments could form. Here, we see that kerolite precipitation can also favor fossilization in this kind of environment. The onset of frustule dissolution increases the local activity of silicic acid, which, in presence of high activities of Mg^{2+} and OH^{-} as encountered in these alkaline lakes, favors kerolite precipitation.

We also observed numerous coccoid and filamentous microbial cells, sometimes at high densities, fossilized by kerolite. The poor crystallinity/small size of the mineral phase likely favored such an exquisite preservation of the morphology of the cells down to the nm-scale. Microbial cell fossils were usually filled with kerolite but were occasionally empty. They were surrounded by kerolite and only an electron transparent space outlined them. This space may correspond spatially to former cell walls. FIB-tomography, TEM, and STXM suggested that this space was sometimes empty. This may be due either to preferential milling by FIB or to the presence of a genuine porosity resulting from the degradation of the cell wall of the microorganisms. Such an intimate association of kerolite with microbial cells may result from a permineralization of the cells under chemical conditions favorable to kerolite precipitation as shown in these lakes. In Mono Lake microbialites, Souza-Egipsy et al. (2005) argued that post-mortem processes led to the precipitation of Mg-silicate on microorganisms. In our study it is not clear if the precipitation of kerolite occurred when microorganisms were alive or after their death. Several mechanisms are possible and will have to be further studied by experimental studies. Living microbes may induce kerolite precipitation, hence their fossilization, by enhancing supersaturation with kerolite within the biofilm, e.g., by increasing pH locally. Several metabolisms populating microbialites tend to increase pH, such as oxygenic and anoxygenic photosynthesis (Dupraz et al., 2009; Saghaï et al., 2015). Alternatively, dead or living cells may decrease the energy barrier to kerolite nucleation by providing cell surfaces on which heterogeneous nucleation occurs.

Burne et al. (2014) observed similar authigenic Mg-silicates in modern thrombolites from Lake Clifton (Western Australia). They suggested that organo-mineralization of biofilms by Mg-silicates was a systematic first step in microbialite formation, followed by abiotic aragonite replacement inducing a loss of the biogenic features visible in the silicates. In our study, we observed consistently patches of Ca-carbonates

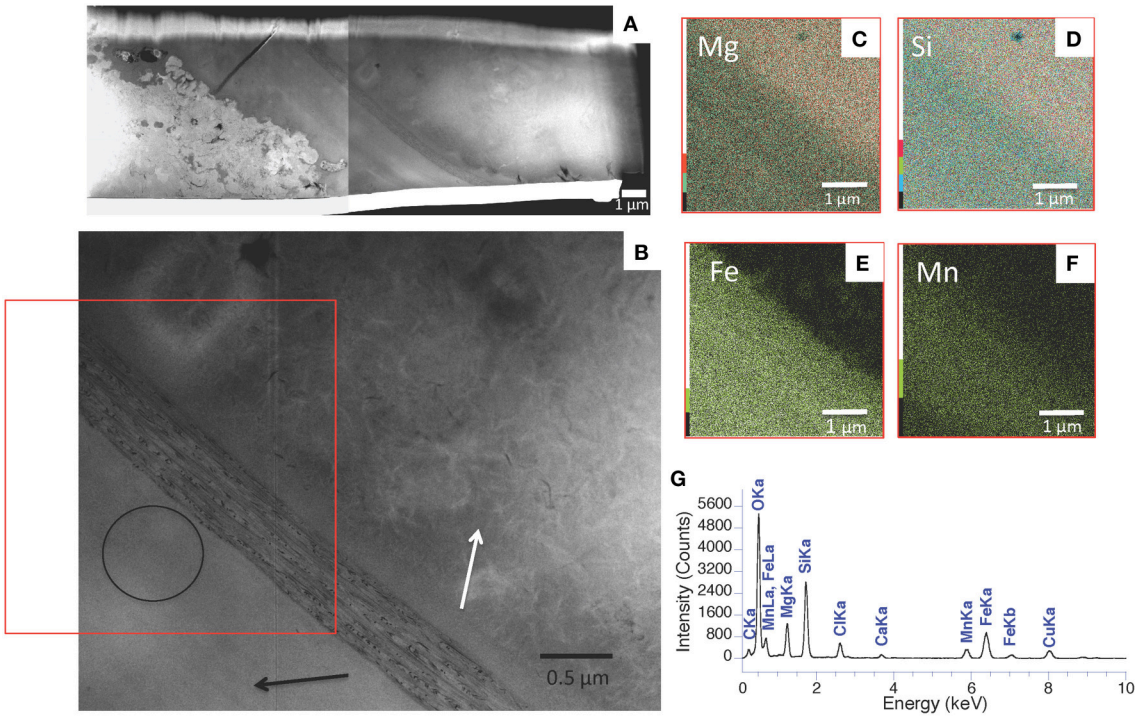

FIGURE 12 | STEM-EDXS analyses of a FIB foil extracted from Atexcac microbialite. (A) HAADF STEM images of the FIB foil extracted from the area shown in **Figure 11** and Figure S8; **(B)** STEM image showing several areas composed of a poorly crystalline silicate phase characterized from one side by a fibrous texture (white arrow) and from the other side by a smooth texture (black arrow); **(C–F)** STEM-EDXS mapping of magnesium **(C)**, silicon **(D)**, iron **(E)**, and manganese **(F)** corresponding to the area marked by a rectangle on **(B)**; **(G)** EDXS spectrum corresponding to the area circled on **(B)**.

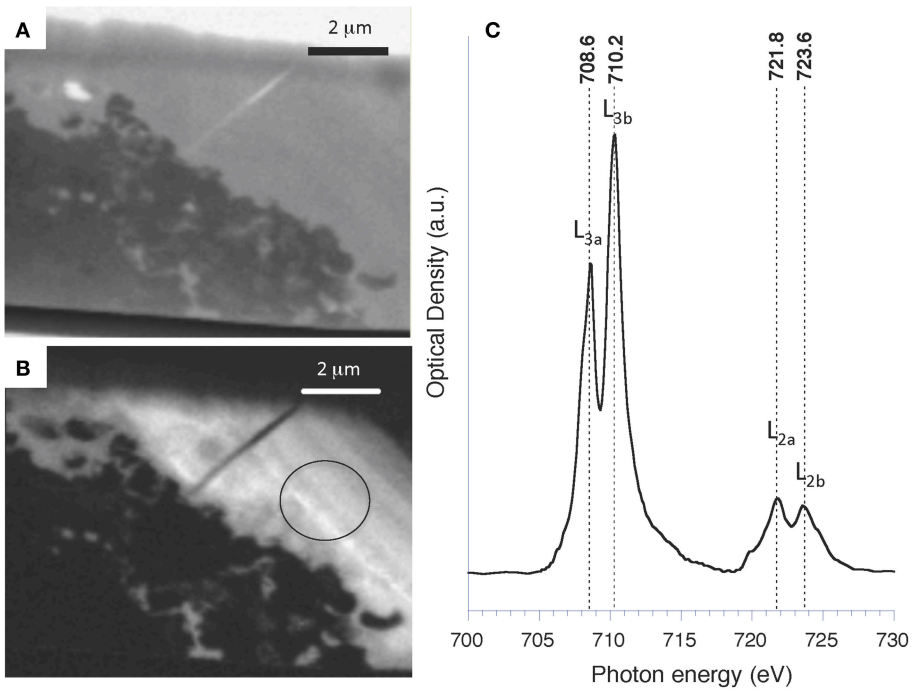

FIGURE 13 | STXM analyses at the Fe $L_{2,3}$-edges of Atexcac microbialite FIB foil shown in Figure 12A. (A) STXM image taken at 700 eV (below the Fe $L_{2,3}$-edge); **(B)** Iron map obtained by subtracting an optical density converted image at 700 eV from an OD-converted image taken at 710 eV; **(C)** XANES spectrum at the Fe $L_{2,3}$-edges from the area circled on **(B)**.

(mainly aragonite) growing in a Mg-silicate matrix. However, we sometimes observed remnants of cells in Ca-carbonates, suggesting that at least some biogenic features can be preserved (Figure S6A). Moreover, Ca-carbonates sometimes form directly as primary phases in these microbialites and not as replacements of Mg-silicates. For example, Couradeau et al. (2013) and Gérard et al. (2013) described the formation of aragonite on Pleurocapsales cells within the biofilms. Here, we show that the Mexican lake solutions are supersaturated with Ca-carbonates (aragonite and calcite) and kerolite. Therefore, the precipitation of one phase instead of the other is a matter of kinetics. Whether precipitation of kerolite vs. Ca-carbonates is favored by major changes of the chemical composition of the lake or local chemical shifts due to microbial activity remains an open question.

Finally, we also detected a systematic intimate association of organic carbon, possibly extracellular polymeric substances (EPS) and/or byproducts of cell degradation, with kerolite. Such an association between EPS and authigenic silicates has been suggested in the past based on textural evidence. Ueshima and Tazaki (2001) hypothesized that EPS may serve as a template for silicate synthesis after an accumulation of Si and Fe ions from the solution. For Léveillé et al. (2000a), dehydration and degradation of a polysaccharide-rich matrix within a biofilm produced a precursor gel, which developed then into poorly crystallized kerolite phase. This organic matrix may impact the aging of the minerals as previously suggested by Lepot et al. (2008) for aragonite. Moreover, some previous studies (e.g., Melendez et al., 2013) have shown that biomarkers can be highly preserved in rocks as old as ∼380 Ma due to microbially induced carbonate precipitation. Therefore, it will be important to decipher in future studies how the organic matrix observed in association with authigenic silicates evolves upon diagenesis and metamorphism and if the microfossils and the organic polymers observed here can be preserved for extended periods such as millions or billions years. In this case, such authigenic silicate occurrences may become an interesting target for studies searching for traces of ancient life. Preservability of these traces upon geological time is not straightforward. Dissolution of kerolite during diagenesis and/or recrystallization into coarser crystals during metamorphism may erase all traces. However, some ancient fossils of soft tissues of metazoans have been preserved by clays in several occurrences, including metamorphic rocks of relatively high grade (Zhang and Briggs, 2007; Galvez et al., 2012; Wacey et al., 2014), supporting the plausibility of fossil preservation by such authigenic silicates.

ACKNOWLEDGMENTS

The research leading to these results has received funding from the European Research Council under the European Union's Seven Framework Program: ERC grants Calcyan (PI: K. Benzerara, Grant Agreement no. 307110) and ProtistWorld (P.I. P. López-García, Grant Agreement no. 322669). Advanced Light Source (ALS) Molecular Environmental Science beamline 11.0.2 is supported by the Office of Science, Office of Basic Energy Sciences, Division of Chemical Sciences, Geosciences, and Biosciences and Materials Sciences Division, U.S. Department of Energy, at the Lawrence Berkeley National Laboratory. The TEM facility at IMPMC was purchased owing to a support by Region Ile-de-France grant SESAME 2000 E 1435. The SEM and FIB facilities at IMPMC were purchased owing to a support by Région Ile de France grant SESAME 2006 I-07-593/R. We thank Laure Cordier (ICP-AES and ion chromatography analyses) and Emmanuelle Raimbault (continuous flow colorimetric analyses and alkalinity measurements) for technical support at IPGP. We thank Franck Bourdelle (Université de Lille) for his assistance with the estimation of the kerolite $Fe^{3+}/\Sigma Fe$ ratios. We thank Stéphane Gaboreau (BRGM) for his help for the analyses of FIB-tomography images.

SUPPLEMENTARY MATERIAL

The Supplementary Material for this article can be found online at: http://journal.frontiersin.org/article/10.3389/feart.2015.00064

REFERENCES

Alcocer, J., and Bernal-Brooks, F. W. (2010). Limnology in mexico. *Hydrobiologia* 644, 15–68. doi: 10.1007/s10750-010-0211-1

Allen, M. A., Goh, F., Burns, B. P., and Neilan, B. A. (2009). Bacterial, archaeal and eukaryotic diversity of smooth and pustular microbial mat communities in the hypersaline lagoon of Shark Bay. *Geobiology* 7, 82–96. doi: 10.1111/j.1472-4669.2008.00187.x

Allwood, A. C., Walter, M. R., Kamber, B. S., Marshall, C. P., and Burch, I. W. (2006). Stromatolite reef from the early Archaean era of Australia. *Nature* 441, 714–718. doi: 10.1038/nature04764

Andres, M. S., Sumner, D. Y., Reid, R. P., and Swart, P. K. (2006). Isotopic fingerprints of microbial respiration in aragonite from Bahamian stromatolites. *Geology* 34, 973–976. doi: 10.1130/G22859A.1

Armienta, M. A., Vilaclara, G., De la Cruz-Reyna, S., Ramos, S., Ceniceros, N., Cruz, O., et al. (2008). Water chemistry of lakes related to active and inactive Mexican volcanoes. *J. Volcanol. Geoth. Res.* 178, 249–258. doi: 10.1016/j.jvolgeores.2008.06.019

Arp, G., Reimer, A., and Reitner, J. (2003). Microbialite formation in seawater of increased alkalinity, Satonda Crater Lake, Indonesia. *J. Sediment. Res.* 73, 105–127. doi: 10.1306/071002730105

Arp, G., Thiel, V., Reimer, A., Michaelis, W., and Reitner, J. (1999). Biofilm exopolymers control microbialite formation at thermal springs discharging into the alkaline Pyramid Lake, Nevada, USA. *Sediment. Geol.* 126, 159–176. doi: 10.1016/S0037-0738(99)00038-X

Awramik, S. M., and Buchheim, H. P. (2009). A giant, late archean lake system: the meentheena member (tumbiana formation; fortescue group), Western Australia. *Precambrian Res.* 174, 215–240. doi: 10.1016/j.precamres.2009.07.005

Badaut, D., and Risacher, F. (1983). Authigenic smectite on diatom frustules in Bolivian Saline lakes. *Geochim. Cosmochim. Acta* 47, 363–375. doi: 10.1016/0016-7037(83)90259-4

Ball, J. W., and Nordstrom, D. K. (1991). *User's Manual for WATEQ4F, with Revised Thermodynamic Data Base and Text Cases for Calculating Speciation of Major, Trace, and Redox Elements in Natural Waters*, U. S. Geological Survey.

Baumgartner, L. K., Spear, J. R., Buckley, D. H., Pace, N. R., Reid, R. P., Dupraz, C., et al. (2009). Microbial diversity in modern marine stromatolites, Highborne

Cay, Bahamas. *Environ. Microbiol.* 11, 2710–2719. doi: 10.1111/j.1462-2920.2009.01998.x

Benzerara, K., Meibom, A., Gautier, Q., Kaźmierczak, J., Stolarski, J., Menguy, N., et al. (2010). Nanotextures of aragonite in stromatolites from the quasi-marine Satonda crater lake, Indonesia. *Geol. Soc. Lond. Spec. Publ.* 336, 211–224. doi: 10.1144/SP336.10

Benzerara, K., Menguy, N., López-García, P., Yoon, T.-H., Kazmierczak, J., Tyliszczak, T., et al. (2006). Nanoscale detection of organic signatures in carbonate microbialites. *Proc. Natl. Acad. Sci. U.S.A.* 103, 9440–9445. doi: 10.1073/pnas.0603255103

Benzerara, K., Yoon, T. H., Tyliszczak, T., Constantz, B., Spormann, A. M., and Brown, G. E. (2004). Scanning transmission X-ray microscopy study of microbial calcification. *Geobiology* 2, 249–259. doi: 10.1111/j.1472-4677.2004.00039.x

Bernard, S., Horsfield, B., Schulz, H.-M., Schreiber, A., Wirth, R., Anh Vu, T. T., et al. (2010). Multi-scale detection of organic and inorganic signatures provides insights into gas shale properties and evolution. *Chemie Erde Geochem.* 70(Suppl. 3), 119–133. doi: 10.1016/j.chemer.2010.05.005

Bluhm, H., Andersson, K., Araki, T., Benzerara, K., Brown, G. E., Dynes, J. J., et al. (2006). Soft X-ray microscopy and spectroscopy at the molecular environmental science beamline at the Advanced Light Source. *J. Electron Spectros. Relat. Phenomena* 150, 86–104. doi: 10.1016/j.elspec.2005.07.005

Bohacs, K. M., Carroll, A. R., Neal, J. E., and Mankiewicz, P. J. (2000). "Lake-basin type, source potential, and hydrocarbon character: an integrated sequence-stratigraphic-geochemical framework," in *Lake Basins through Space and Time: AAPG Studies in Geology,* Vol. 46, eds E. H. Gierlowski-Kordesch and K. R. Kelts (Tulsa, OK: AAPG), 3–34.

Bontognali, T. R., Sessions, A. L., Allwood, A. C., Fischer, W. W., Grotzinger, J. P., Summons, R. E., et al. (2012). Sulfur isotopes of organic matter preserved in 3.45-billion-year-old stromatolites reveal microbial metabolism. *Proc. Natl. Acad. Sci. U.S.A.* 109, 15146–15151. doi: 10.1073/pnas.1207491109

Bontognali, T. R. R., Vasconcelos, C., Warthmann, R. J., Bernasconi, S. M., Dupraz, C., Strohmenger, C. J., et al. (2010). Dolomite formation within microbial mats in the coastal sabkha of Abu Dhabi (United Arab Emirates): Dolomite formation within microbial mats. *Sedimentology* 57, 824–844. doi: 10.1111/j.1365-3091.2009.01121.x

Bourdelle, F., Benzerara, K., Beyssac, O., Cosmidis, J., Neuville, D. R., Brown, G. E., et al. (2013). Quantification of the ferric/ferrous iron ratio in silicates by scanning transmission X-ray microscopy at the Fe L2,3 edges. *Contrib. Mineral. Petrol.* 166, 423–434. doi: 10.1007/s00410-013-0883-4

Bradley, W. H., and Eugster, H. P. (1969). Geochemistry and paleolimnology of the trona deposits and associated authigenic minerals of the Green River Formation of Wyoming. *U.S. Geological Survey Professional Paper 496B*, 71p. Available online at: http://pubs.er.usgs.gov/publication/pp496B

Braithwaite, C. J. R., and Zedef, V. (1994). Living hydromagnesite stromatolites from Turkey. *Sediment. Geol.* 92, 1–5. doi: 10.1016/0037-0738(94)90051-5

Brandes, J. A., Lee, C., Wakeham, S., Peterson, M., Jacobsen, C., Wirick, S., et al. (2004). Examining marine particulate organic matter at sub-micron scales using scanning transmission X-ray microscopy and carbon X-ray absorption near edge structure spectroscopy. *Mar. Chem.* 92, 107–121. doi: 10.1016/j.marchem.2004.06.020

Brindley, G. (1959). X-Ray and electron diffraction data for sepiolite. *Am. Miner.* 44, 495–500.

Brindley, G. W. (1977). The nature of kerolite, its relation to talc and stevensite. *Mineral. Mag.* 41, 443–452. doi: 10.1180/minmag.1977.041.320.04

Buick, R., Dunlop, J. S. R., and Groves, D. I. (1981). Stromatolite recognition in ancient rocks: an appraisal of irregularly laminated structures in an Early Archaean chert-barite unit from North Pole, Western Australia. *Alcheringa* 5, 161–181. doi: 10.1080/03115518108566999

Burne, R. V., and Moore, L. S. (1987). Microbialites: organosedimentary deposits of benthic microbial communities. *Palaios* 2, 241–254. doi: 10.2307/3514674

Burne, R. V., Moore, L. S., Christy, A. G., Troitzsch, U., King, P. L., Carnerup, A. M., et al. (2014). Stevensite in the modern thrombolites of Lake Clifton, Western Australia: a missing link in microbialite mineralization? *Geology* 42, 575–578. doi: 10.1130/G35484.1

Byerly, G. R., Lower, D. R., and Walsh, M. M. (1986). Stromatolites from the 3,300–3,500-Myr Swaziland Supergroup, Barberton Mountain Land, South Africa. *Nature* 319, 489–491. doi: 10.1038/319489a0

Cai, Y., Xue, J., and Polya, D. A. (2007). A Fourier transform infrared spectroscopic study of Mg-rich, Mg-poor and acid leached palygorskites. *Spectrochim. Acta Part A* 66, 282–288. doi: 10.1016/j.saa.2006.02.053

Carrasco-Núñez, G., Ort, M. H., and Romero, C. (2007). Evolution and hydrological conditions of a maar volcano (Atexcac crater, Eastern Mexico). *J. Volcanol. Geoth. Res.* 159, 179–197. doi: 10.1016/j.jvolgeores.2006.07.001

Carteret, C., De La Pierre, M., Dossot, M., Pascale, F., Erba, A., and Dovesi, R. (2013). The vibrational spectrum of CaCO3 aragonite: a combined experimental and quantum-mechanical investigation. *J. Chem. Phys.* 138, 014201. doi: 10.1063/1.4772960

Centeno, C. M., Legendre, P., Beltrán, Y., Alcántara-Hernández, R. J., Lidström, U. E., Ashby, M. N., et al. (2012). Microbialite genetic diversity and composition relate to environmental variables. *FEMS Microbiol. Ecol.* 82, 724–735. doi: 10.1111/j.1574-6941.2012.01447.x

Chan, C. S., Fakra, S. C., Edwards, D. C., Emerson, D., and Banfield, J. F. (2009). Iron oxyhydroxide mineralization on microbial extracellular polysaccharides. *Geochim. Cosmochim. Acta* 73, 3807–3818. doi: 10.1016/j.gca.2009.02.036

Chen, J., and Lee, J.-H. (2014). Current Progress on the Geological Record of Microbialites and Microbial Carbonates. *Acta Geol. Sin. Engl. Ed.* 88, 260–275. doi: 10.1111/1755-6724.12196

Cibin, G., Marcelli, A., Mottana, A., Giuli, G., DellaVentura, G., Romano, C., et al. (2003). "Magnesium X-ray absorption near-edge structure (XANES) sprectroscopy on synthetic model compounds and minerals," in *19th International Conference on X-ray and Inner Shell Processes,* Vol. 32, eds A. Bianconi, A. Marcelli, and N. L. Saini (Frascati: INFN), 95–150.

Cosmidis, J., and Benzerara, K. (2014). "Soft x-ray scanning transmission spectromicroscopy," in *Biomineralization Sourcebook: Characterization of Biominerals and Biomimetic Materials*, eds E. DiMasi and L. B. Gower (New York, NY: CRC Press), 115–133.

Couradeau, E., Benzerara, K., Gérard, E., Estève, I., Moreira, D., Tavera, R., et al. (2013). Cyanobacterial calcification in modern microbialites at the submicrometer scale. *Biogeosciences* 10, 5255–5266. doi: 10.5194/bg-10-5255-2013

Couradeau, E., Benzerara, K., Moreira, D., Gérard, E., Kaźmierczak, J., Tavera, R., et al. (2011). Prokaryotic and Eukaryotic community structure in field and cultured microbialites from the alkaline lake alchichica (Mexico) ed. J. A. Gilbert. *PLoS ONE* 6:e28767. doi: 10.1371/journal.pone.0028767

Darragi, F., and Tardy, Y. (1987). Authigenic trioctahedral smectites controlling pH, alkalinity, silica and magnesium concentrations in alkaline lakes. *Chem. Geol.* 63, 59–72. doi: 10.1016/0009-2541(87)90074-X

Decho, A. W., Visscher, P. T., and Reid, R. P. (2005). Production and cycling of natural microbial exopolymers (EPS) within a marine stromatolite. *Palaeogeogr. Palaeoclimatol. Palaeoecol.* 219, 71–86. doi: 10.1016/j.palaeo.2004.10.015

Dupraz, C., Reid, R. P., Braissant, O., Decho, A. W., Norman, R. S., and Visscher, P. T. (2009). Processes of carbonate precipitation in modern microbial mats. *Earth Sci. Rev.* 96, 141–162. doi: 10.1016/j.earscirev.2008.10.005

Dyni, J. R. (1976). Trioctahedral smectite in the green river formation, Duchesne County, Utah. *U.S. Geological Survey Professional Paper 967*, 14 p. Available online at: http://pubs.er.usgs.gov/publication/pp967

Farmer, V. C. (1974). *The Infrared Spectra of Minerals*. London: The Mineralogical Society.

Ferrari, L., Orozco-Esquivel, T., Manea, V., and Manea, M. (2012). The dynamic history of the trans-mexican volcanic belt and the mexico subduction zone. *Tectonophysics* 522–523, 122–149. doi: 10.1016/j.tecto.2011.09.018

Forel, M.-B., Crasquin, S., Kershaw, S., and Collin, P.-Y. (2013). In the aftermath of the end-Permian extinction: the microbialite refuge? *Terra Nova* 25, 137–143. doi: 10.1111/ter.12017

Furquim, S. A. C., Graham, R. C., Barbiero, L., de Queiroz Neto, J. P., and Vallès, V. (2008). Mineralogy and genesis of smectites in an alkaline-saline environment of Pantanal wetland, Brazil. *Clays Clay Miner.* 56, 579–595. doi: 10.1346/CCMN.2008.0560511

Galvez, M. E., Beyssac, O., Benzerara, K., Bernard, S., Menguy, N., Cox, S. C., et al. (2012). Morphological preservation of carbonaceous plant fossils in

blueschist metamorphic rocks from New Zealand. *Geobiology* 10, 118–129. doi: 10.1111/j.1472-4669.2011.00316.x

Gérard, E., Ménez, B., Couradeau, E., Moreira, D., Benzerara, K., Tavera, R., et al. (2013). Specific carbonate–microbe interactions in the modern microbialites of Lake Alchichica (Mexico). *ISME J.* 7, 1997–2009. doi: 10.1038/ismej.2013.81

Goh, F., Allen, M. A., Leuko, S., Kawaguchi, T., Decho, A. W., Burns, B. P., et al. (2009). Determining the specific microbial populations and their spatial distribution within the stromatolite ecosystem of Shark Bay. *ISME J.* 3, 383–396. doi: 10.1038/ismej.2008.114

Gran, G. (1952). Determination of the equivalence point in potentiometric titrations. Part, I. I. *Analyst* 77, 661–671.

Guo, X., and Chafetz, H. S. (2012). Large tufa mounds, Searles Lake, California. *Sedimentology* 59, 1509–1535. doi: 10.1111/j.1365-3091.2011.01315.x

Hammer, U. T. (1986). *Saline Lake Ecosystems of the World*. Dordrecht: Dr W Junk Publishers.

Harris, P. M., Ellis, J., and Purkis, S. J. (2013). Assessing the extent of carbonate deposition in early rift settings. *Am. Assoc. Pet. Geol. Bull.* 97, 27–60. doi: 10.1306/06121212003

Hitchcock, A. (2012). *aXis 2000 – Analysis of X-ray Images and Spectra*. Available online at: http://unicorn.mcmaster.ca/aXis2000.html [Accessed February 16, 2012].

Hofmann, H. J. (2000). "Archean stromatolites as microbial archives," in *Microbial Sediments,* eds R. E. Riding and S. M. Awramik (Berlin: Springer), 315–327.

Huang, C., and Kerr, P. (1960). Infrared study of the carbonate minerals. *Am. Miner.* 45, 311–324.

Jones, B., and Peng, X. (2014). Signatures of biologically influenced $CaCO_3$ and Mg-Fe silicate precipitation in hot springs: case study from the ruidian geothermal area, western Yunnan Province, China ed. M. Pedley. *Sedimentology* 61, 56–89. doi: 10.1111/sed.12043

Jones, B. F. (1986). "Clay mineral diagenesis in lacustrine sediments," in *Studies in Diagenesis,* ed F. A. Mumpton (Washington, DC: U.S. Geological Survey USGS Bulletin 1578), 291–300.

Kaufman, A. J. (1996). Geochemical and mineralogic effects of contact metamorphism on banded iron-formation: an example from the Transvaal Basin, South Africa. *Precambrian Res.* 79, 171–194.

Kaźmierczak, J., Kempe, S., Kremer, B., López-García, P., Moreira, D., and Tavera, R. (2011). Hydrochemistry and microbialites of the alkaline crater lake Alchichica, Mexico. *Facies* 57, 543–570. doi: 10.1007/s10347-010-0255-8

Kempe, S., Kaźmierczak, J., Landmann, G., Konuk, T., Reimer, A., and Lipp, A. (1991). Largest known microbialites discovered in Lake Van, Turkey. *Nature* 349, 605–608.

Knoll, A. H., Wörndle, S., and Kah, L. C. (2013). Covariance of microfossil assemblages and microbialite textures across an upper mesoproterozoic carbonate platform. *Palaios* 28, 453–470. doi: 10.2110/palo.2013.p13-005r

Konhauser, K. O., Amskold, L., Lalonde, S. V., Posth, N. R., Kappler, A., and Anbar, A. (2007). Decoupling photochemical Fe(II) oxidation from shallow-water BIF deposition. *Earth Planet. Sci. Lett.* 258, 87–100. doi: 10.1016/j.epsl.2007.03.026

Lee, J.-H., Chen, J., and Chough, S. K. (2010). Paleoenvironmental implications of an extensive maceriate microbialite bed in the furongian chaomidian formation, Shandong Province, China. *Palaeogeogr. Palaeoclimatol. Palaeoecol.* 297, 621–632. doi: 10.1016/j.palaeo.2010.09.012

Lepot, K., Benzerara, K., Brown, G. E., and Philippot, P. (2008). Microbially influenced formation of 2,724-million-year-old stromatolites. *Nat. Geosci.* 1, 118–121. doi: 10.1038/ngeo107

Lepot, K., Benzerara, K., Rividi, N., Cotte, M., Brown, G. E., and Philippot, P. (2009). Organic matter heterogeneities in 2.72Ga stromatolites: Alteration versus preservation by sulfur incorporation. *Geochim. Cosmochim. Acta* 73, 6579–6599. doi: 10.1016/j.gca.2009.08.014

Léveillé, R. J., Fyfe, W. S., and Longstaffe, F. J. (2000a). Geomicrobiology of carbonate–silicate microbialites from Hawaiian basaltic sea caves. *Chem. Geol.* 169, 339–355. doi: 10.1016/S0009-2541(00)00213-8

Léveillé, R. J., Fyfe, W. S., and Longstaffe, F. J. (2000b). Unusual secondary Ca-Mg-carbonate-kerolite deposits in basaltic caves, Kauai, Hawaii. *J. Geol.* 108, 613–621. doi: 10.1086/314417

Léveillé, R. J., Longstaffe, F. J., and Fyfe, W. S. (2002). Kerolite in carbonate-rich speleothems and microbial deposits from basaltic caves, Kauai, Hawaii. *Clays Clay Miner.* 50, 514–524. doi: 10.1346/000986002320514235

Léveillé, R. J., Longstaffe, F. J., and Fyfe, W. S. (2007). An isotopic and geochemical study of carbonate-clay mineralization in basaltic caves: abiotic versus microbial processes. *Geobiology* 5, 235–249. doi: 10.1111/j.1472-4669.2007.00109.x

Li, D., Peng, M., and Murata, T. (1999). Coordination and local structure of magnesium in silicate minerals and glases: Mg K-edge XANES. *Can. Mineral.* 37, 199–206.

Li, J., Benzerara, K., Bernard, S., and Beyssac, O. (2013). The link between biomineralization and fossilization of bacteria: Insights from field and experimental studies. *Chem. Geol.* 359, 49–69. doi: 10.1016/j.chemgeo.2013.09.013

Li, J., Bernard, S., Benzerara, K., Beyssac, O., Allard, T., Cosmidis, J., et al. (2014). Impact of biomineralization on the preservation of microorganisms during fossilization: an experimental perspective. *Earth Planet. Sci. Lett.* 400, 113–122. doi: 10.1016/j.epsl.2014.05.031

Logan, B. (1961). Cryptozoon and associate stromatolites from the recent, Shark Bay, Western-Australia. *J. Geol.* 69, 517–533. doi: 10.1086/626769

López-García, P., Kazmierczak, J., Benzerara, K., Kempe, S., Guyot, F., and Moreira, D. (2005). Bacterial diversity and carbonate precipitation in the giant microbialites from the highly alkaline Lake Van, Turkey. *Extremophiles* 9, 263–274. doi: 10.1007/s00792-005-0457-0

Melendez, I., Grice, K., and Schwark, L. (2013). Exceptional preservation of Palaeozoic steroids in a diagenetic continuum. *Sci. Rep.* 3:2768. doi: 10.1038/srep02768

Miot, J., Benzerara, K., Obst, M., Kappler, A., Hegler, F., Schädler, S., et al. (2009). Extracellular iron biomineralization by photoautotrophic iron-oxidizing bacteria. *Appl. Environ. Microbiol.* 75, 5586–5591. doi: 10.1128/AEM.00490-09

Mobberley, J. M., Ortega, M. C., and Foster, J. S. (2012). Comparative microbial diversity analyses of modern marine thrombolitic mats by barcoded pyrosequencing. *Environ. Microbiol.* 14, 82–100. doi: 10.1111/j.1462-2920.2011.02509.x

Moore, D. M., and Reynolds, R. C. Jr. (1997). "Sample preparation techniques for clay minerals," in *X-ray Diffraction and the Identification and Analyses of Clay Minerals, 2nd Edn* (Oxford; New York, NY: Oxford University Press), 204–226.

Moreno, E. C., Gregory, T. M., and Brown, W. E. (1968). Preparation and solubility of hydroxyapatite. *J. Res. Natl. Bur. Stand. Phys. Chem.* 72A, 773–782. doi: 10.6028/jres.072A.052

Nayak, P. K., Mohapatra, B. K., Singh, P. P., and Martha, R. K. (2011). Cobalt-bearing grunerite in the metamorphosed banded iron formation in Orissa, India: cobalt bearing grunerite in BIF, Orissa. *Resour. Geol.* 61, 281–289. doi: 10.1111/j.1751-3928.2011.00164.x

Papineau, D., Walker, J. J., Mojzsis, S. J., and Pace, N. R. (2005). Composition and structure of microbial communities from stromatolites of Hamelin Pool in Shark Bay, Western Australia. *Appl. Environ. Microbiol.* 71, 4822–4832. doi: 10.1128/AEM.71.8.4822-4832.2005

Perry, C. C. (2003). "Silicification: the processes by which organisms capture and mineralize silica" in *Reviews in Mineralogy and Geochemistry*, *Biomineralization*, Vol. 54, ed J. J. Rosso (Chantilly, VA: Mineralogical Society of America, Geochemical Society), 291–327.

Plummer, L. N., and Busenberg, E. (1982). The solubilities of calcite, aragonite and vaterite in CO2-H2O solutions between 0 and 90°C, and an evaluation of the aqueous model for the system CaCO3-CO2-H2O. *Geochim. Cosmochim. Acta* 46, 1011–1040. doi: 10.1016/0016-7037(82)90056-4

Power, I. M., Wilson, S. A., Dipple, G. M., and Southam, G. (2011). Modern carbonate microbialites from an asbestos open pit pond, Yukon, Canada: Modern carbonate microbialites from an asbestos open pit pond. *Geobiology* 9, 180–195. doi: 10.1111/j.1472-4669.2010.00265.x

Reid, R. P., James, N. P., Macintyre, I. G., Dupraz, C. P., and Burne, R. V. (2003). Shark Bay stromatolites: microfabrics and reinterpretation of origins. *Facies* 49, 299–324. doi: 10.1007/s10347-003-0036-8

Reimer, A., Landmann, G., and Kempe, S. (2009). Lake Van, eastern anatolia, hydrochemistry and history. *Aquat. Geochem.* 15, 195–222. doi: 10.1007/s10498-008-9049-9

Robie, R. A., and Hemingway, B. S. (1973). The enthalpies of formation of nesquehonite, MgCO3-3HA and hydromagnesite, 5MgO.4CO2-5H2O. *U.S. Geol. Surv. J. Res.* 1, 543–545.

Saghaï, A., Zivanovic, Y., Zeyen, N., Moreira, D., Benzerara, K., Deschamps, P., et al. (2015). Metagenome-based diversity analyses suggest a significant contribution of non-cyanobacterial lineages to carbonate precipitation in modern microbialites. *Front. Microbiol.* 6:797. doi: 10.3389/fmicb.2015.00797

Saint Martin, J.-P. (2010). The Girvanella-like remains from Messinian marine deposits (Sardinia, Italy): Lagerstätten paradigm for microbial biota? *Annal. Paléontol.* 96, 33–50. doi: 10.1016/j.annpal.2010.10.002

Sánchez del Río, M., Suárez, M., García Romero, E., Alianelli, L., Felici, R., Martinetto, P., et al. (2005). Mg K-edge XANES of sepiolite and palygorskite. *Nucl. Instr. Methods Phys. Res. Sect. B* 238, 55–60. doi: 10.1016/j.nimb.2005.06.018

Sánchez-Navas, A., Martín-Algarra, A., and Nieto, F. (1998). Bacterially-mediated authigenesis of clays in phosphate stromatolites. *Sedimentology* 45, 519–533. doi: 10.1046/j.1365-3091.1998.00157.x

Schwertmann, U. (1991). Solubility and dissolution of iron oxides. *Plant Soil* 130, 1–25. doi: 10.1007/BF00011851

Seard, C., Camoin, G., Rouchy, J.-M., and Virgone, A. (2013). Composition, structure and evolution of a lacustrine carbonate margin dominated by microbialites: Case study from the Green River formation (Eocene; Wyoming, USA). *Palaeogeogr. Palaeoclimatol. Palaeoecol.* 381–382, 128–144. doi: 10.1016/j.palaeo.2013.04.023

Souza-Egipsy, V., Wierzchos, J., Ascaso, C., and Nealson, K. H. (2005). Mg–silica precipitation in fossilization mechanisms of sand tufa endolithic microbial community, Mono Lake (California). *Chem. Geol.* 217, 77–87. doi: 10.1016/j.chemgeo.2004.12.004

Stoessell, R. K. (1988). 25°C and 1 atm dissolution experiments of sepiolite and kerolite. *Geochim. Cosmochim. Acta* 52, 365–374. doi: 10.1016/0016-7037(88)90092-0

Stüeken, E. E., Buick, R., and Schauer, A. J. (2015). Nitrogen isotope evidence for alkaline lakes on late Archean continents. *Earth Planet. Sci. Lett.* 411, 1–10. doi: 10.1016/j.epsl.2014.11.037

Tank, R. W. (1972). Clay minerals of the Green River Formation (Eocene) of Wyoming. *Clay Miner.* 9, 297–308. doi: 10.1180/claymin.1972.009.3.05

Thomazo, C., Ader, M., and Philippot, P. (2011). Extreme 15N-enrichments in 2.72-Gyr-old sediments: evidence for a turning point in the nitrogen cycle: Extreme 15N-enrichments in 2.72-Gyr-old sediments. *Geobiology* 9, 107–120. doi: 10.1111/j.1472-4669.2011.00271.x

Tosca, N. J., and Masterson, A. L. (2014). Chemical controls on incipient Mg-silicate crystallization at 25°C: Implications for early and late diagenesis. *Clay Miner.* 49, 165–194. doi: 10.1180/claymin.2014.049.2.03

Tosca, N. J., Macdonald, F. A., Strauss, J. V., Johnston, D. T., and Knoll, A. H. (2011). Sedimentary talc in Neoproterozoic carbonate successions. *Earth Planet. Sci. Lett.* 306, 11–22. doi: 10.1016/j.epsl.2011.03.041

Trcera, N., Cabaret, D., Rossano, S., Farges, F., Flank, A.-M., and Lagarde, P. (2009). Experimental and theoretical study of the structural environment of magnesium in minerals and silicate glasses using X-ray absorption near-edge structure. *Phys. Chem. Minerals* 36, 241–257. doi: 10.1007/s00269-008-0273-z

Ueshima, M., and Tazaki, K. (2001). Possible role of microbial polysaccharides in nontronite formation. *Clays Clay Miner.* 49, 292–299. doi: 10.1346/CCMN.2001.0490403

Van Kranendonk, M., Philippot, P., Lepot, K., Bodorkos, S., and Pirajno, F. (2008). Geological setting of Earth's oldest fossils in the ca. 3.5Ga Dresser Formation, Pilbara Craton, Western Australia. *Precambrian Res.* 167, 93–124. doi: 10.1016/j.precamres.2008.07.003

Vilaclara, G., Chávez, M., Lugo, A., González, H., and Gaytán, M. (1993). Comparative description of crater-lakes basic chemistry in Puebla State, Mexico. *Verhandlungen Internationale Vereinigung für Theoretische Angewandte Limnologie* 25, 435–440.

Wacey, D., Saunders, M., Roberts, M., Menon, S., Green, L., Kong, C., et al. (2014). *Enhanced Cellular Preservation by Clay Minerals in 1 Billion-year-old lakes*. Scientific Reports 4. Available online at: http://www.nature.com/doifinder/10.1038/srep05841 [Accessed October 20, 2014].

Walter, M. R., Buick, R., and Dunlop, J. S. R. (1980). Stromatolites 3,400–3,500 Myr old from the North Pole area, Western Australia. *Nature* 284, 443–445. doi: 10.1038/284443a0

White, W. B. (1971). Infrared characterization of water and hydroxyl ion in the basic magnesium carbonate minerals. *Am. Mineral.* 56, 46–53.

Whitney, G., and Eberl, D. D. (1982). Mineral paragenesis in a talc-water experimental hydrothermal system. *Am. Mineral.* 67, 944–949.

Wilkins, R., and Ito, J. (1967). Infrared spectra of some synthetic talcs. *Am. Mineral.* 52, 1649–1660.

William Schopf, J. (2011). The paleobiological record of photosynthesis. *Photosyn. Res.* 107, 87–101. doi: 10.1007/s11120-010-9577-1

Wollast, R. (1974). "The silica problem," in *The Sea,* Vol. 5, ed E. D. Goldberg (New York, NY: Wiley-Interscience), 359–425.

Wollast, R., Mackenzie, F. T., and Bricker, O. P. (1968). Experimental precipitation and genesis of sepiolite at earth-surface conditions. *Am. Mineral.* 53, 1645–1661.

Wright, V. P., and Barnett, A. J. (2015). "An abiotic model for the development of textures in some South Atlantic early Cretaceous lacustrine carbonates," in *Microbial Carbonates in Space and Time: Implications for Global Exploration and Production,* eds D. W. J. Bosence, K. A. Gibbons, D. P. le Heron, W. A. Morgan, T. Pritchard, and B. A. Vining (London: Geological Society, Special Publications), 418.

Zhang, X., and Briggs, D. E. G. (2007). The nature and significance of the appendages of Opabinia from the Middle Cambrian Burgess Shale. *Lethaia* 40, 161–173. doi: 10.1111/j.1502-3931.2007.00013.x

Conflict of Interest Statement: The authors declare that the research was conducted in the absence of any commercial or financial relationships that could be construed as a potential conflict of interest.